SAND2020-5664J

Topological Effects on Separation of Alkane Isomers in Metal–Organic Frameworks

N. Scott Bobbitt[1], Andrew S. Rosen[2], Randall Q. Snurr[2*]

1. Sandia National Laboratories, Albuquerque, New Mexico, 87185

2. Department of Chemical and Biological Engineering, Northwestern University, Evanston, Illinois, 60208

Abstract

Polymorphism in metal–organic frameworks (MOFs) means that the same chemical building blocks (nodes and linkers) can be used to construct isomeric MOFs with different topological networks. The choice of topology can substantially impact the pore network of the MOF, changing the sizes and shapes of the pores, which has implications for adsorption and separation applications. In this work, we look at the influence of topology in 38 polymorphic MOFs on the separation of linear and branched C4-C6 alkane isomers, a separation of great importance to the petrochemical industry. We find that the MOF Cu_2(1,4-benzenedicarboxylate) in **nbo** topology (nbo-Cu_2BDC) has particularly high affinity for linear alkanes due to its small pore size, which excludes the branched isomers. Upon studying this MOF in further detail, we find that it can take either of two conformations: a cubic conformation, which is typical of **nbo** MOFs, and a unique star conformation that contains 1D triangular and hexagonal channels. The determination of which conformation the MOF will adopt depends on steric effects between the nodes and linkers.

1: Introduction

Metal–organic frameworks (MOFs) are porous, crystalline materials made from inorganic nodes connected by organic linkers. They can be constructed from many different combinations of nodes and linkers, and owing to this modularity, MOFs have been a popular target for high-throughput computational screening studies based on databases of hypothetical MOF structures built from a set of preselected nodes and linkers.[1-3] These studies have often focused on identifying specific high-performing candidates for a given application or developing structure-property relationships based on textural properties, such as pore volume and surface area. MOFs offer a high level of tunability in this regard. For example, one can choose a longer or shorter linker to produce the desired pore size for a given application of interest,[4-5] or use functional groups to increase the number of binding sites for a target adsorbate.[6]

Less attention, however, has been given to the effect of MOF topology on adsorption behavior. Beyond the choice of inorganic and organic building blocks, MOFs can be defined by their topological network (i.e. the network of connectivity between the nodes and edges). MOFs can exhibit a form of polymorphism in which unique MOFs can be built from the same nodes and linkers yet are connected in different topologies. Polymorphic MOFs are essentially isomers: they have the same chemical formula and contain all the same atoms in the same ratios, but they are arranged in a different crystallographic pattern.[7-8]

**Corresponding author: snurr@northwestern.edu*

One example of polymorphism can be found in the **tbo** and **pto** Cu-paddlewheel MOFs reported by Zhu et al.[9] They found that the framework TCM-8 in the **tbo** topology has significantly higher pore volume and surface area than its **pto** counterpart. Controlling topology during MOF synthesis is a challenging problem, but some progress has been made in topological control using modulators and varying reaction conditions.[10-13] There remains a need for more research into synthetic control of topology because the choice of topology can provide another adjustable variable in the effort to tune MOF properties for a specific application.

Here we explore the effects of topology on the separation of linear and branched C4-C6 alkane isomers. This separation is of notable industrial importance[14-15] because branched alkanes, especially of hexane, are key components in high-octane gasoline. The research octane number is a measure of the combustion properties of the gasoline compared to a mixture of *n*-heptane and iso-octane under engine operation conditions. Generally, gasoline with higher research octane number reduces engine knocking and improves engine performance. The research octane number of *n*-hexane is 25, whereas the research octane numbers of the hexane isomers 2,2-dimethylbutane and 2,3-dimethylbutane are 92 and 104, respectively.[16-17] In order to enrich gasoline to a higher octane number, alkane streams are passed through an isomerization process[18] followed by a separation to remove the desirable dibranched methylbutanes. The remaining linear and monobranched isomers are recycled back to the isomerization process. These separations are often achieved using distillation, but adsorption-based separation methods using MOFs could offer an appealing, less energy-intensive alternative. One of the earliest computational studies of linear and branched alkane separations in MOFs was done by Jiang and Sandler in IRMOF-1.[19] Other studies have considered alkane separations in several MOFs,[14, 20-24] as well as carbon nanotubes[25-26] and zeolites[27] for this application, but the specific effects of the topology have not been discussed in depth.

In this work, we study the adsorption of all ten C4, C5, and C6 isomers in 38 MOFs. These MOFs consist of four "families" of polymorphs (we consider a polymorph family to be a group of topologies that form polymorphs with each other), and in each family we consider MOFs with 3 or 4 different linkers. We identify one MOF made of the Cu_2 paddlewheel node and 1,4-benzenedicarboxylate linker in the **nbo** topology that demonstrates exceptionally high selectivity for linear alkanes, and we further explore two different geometrical conformations for this MOF.

2: Methods

2.1 Selection of MOFs

The 38 MOFs considered in this work were taken from the database of Colón and Gómez-Gualdrón.[28] These MOFs were constructed *in silico* using the ToBaCCo algorithm. ToBaCCo creates porous crystals by assembling (organic and inorganic) nodes and edges based on a predetermined topological map. For details about how this algorithm works, see Colón and Gómez-Gualdrón.[28] We used the energy-minimized MOF structures available from ToBaCCo. In the original work, structural minimizations of all MOFs were done in Materials Studio[29] using the Universal Force Field[30] with no partial atomic charges. In this work, we studied some MOFs in further detail using periodic density functional theory (DFT).

MOFs with identical chemical formulas and different topologies were distinguished using the MOFid algorithm developed by Bucior et al.[31] The MOFids and MOFkeys for all MOFs discussed in this work are listed in Supplemental Table 1. We found 2308 groups of polymorphs for a total of 5559 polymorphic

MOFs in the ToBaCCo database. Many of these MOFs are analogues made with different length edges (e.g., adding an extra alkyne spacer or phenyl ring). To reduce the number of MOFs further, we chose only 3-4 edges for each polymorph family. The four distinct polymorph families chosen in this work include the following sets of topologies: **dia**/**lcs**/**sod**, **lvt**/**nbo**/**rhr**, **tbo**/**pto**, and **ssa**/**ssb.** Two families included three topologies (**dia**/**lcs**/**sod** and **lvt**/**nbo**/**rhr**)**.** We also included the **tbo**/**pto** family because there has been recent experimental research on controlling the synthesis of MOFs in these topologies. [9] We included the **ssa**/**ssb** family to increase the diversity of linkers used in our study. These topologies use a series of "bent" edges that are incompatible with the straight ditopic edges used in the other eight topologies included in this work.

The specific building blocks used to construct the MOFs are shown in Figure 1 and Figure 2. Due to the way the ToBaCCo algorithm constructs MOF structures, some MOFs have both inorganic nodes and organic nodes. The organic nodes can be considered a component of the organic linker, but they are labeled as nodes for the purpose of mapping the crystal to the topology because the vertices in the topological graph can be either inorganic or organic in nature. In this work we refer to the ditopic organic building blocks as "edges" and the entire organic building blocks (including the edges and organic nodes) as "linkers." We have retained the labels for the organic edges used by Colón and Gómez-Gualdrón but changed the labels of the nodes to Metal Nodes 1 and 2 and Organic Nodes 1 and 2 for simplicity. Edges can connect to either organic or inorganic nodes, and an edge connected to two inorganic nodes constitutes a linker.

The **lvt/nbo/rhr** family is made from $Cu_2(COO)_4$ nodes (Figure 1, Metal Node 1, commonly known as a Cu-paddlewheel node) and edges L3, L12, L20, and L24 (Figure 2). We will also discuss the **nbo** variant of this family made with a Cu-paddlewheel node (Metal Node 1) and edge L22 (Figure 11), although this MOF was not part of the 38 used in the initial screening. The family of **dia**/**lcs**/**sod** MOFs are made from $ZnN_4(C_5H_4)_4$ nodes (Figure 1, Metal Node 2; in this work and the ToBaCCo construction algorithm, the C_5NH_4 rings are considered part of the inorganic node). The edges used for this family are L3, L12, L20, and L24 (Figure 2). The **tbo/pto** family is made using Organic Node 1, Metal Node 1 (Figure 1), and edges L3, L12, L20, and L24 (Figure 2). The **ssa/ssb** family is made from Organic Node 2, Metal Node 1 (Figure 1), and edges L4, L15, and L21 (Figure 2). The **ssa/ssb** family uses different edges because these topologies are not compatible with the straight shape of edges L3, L12, L20, and L24. Diagrams of the topological nets used in this work are shown in Supplemental Figure 1. The structure files for all the MOFs discussed in this work are available in the Supplemental Information.

In this paper, we will refer to the MOFs as their respective topology and edge. In this work, all of the MOFs of a given topology contain the same inorganic nodes; therefore, specifying the topology and edge is sufficient to indicate a unique MOF. For example, the MOF made of Metal Node 2 and edge L20 in the **dia** topology is called (in this work) "dia_L20."

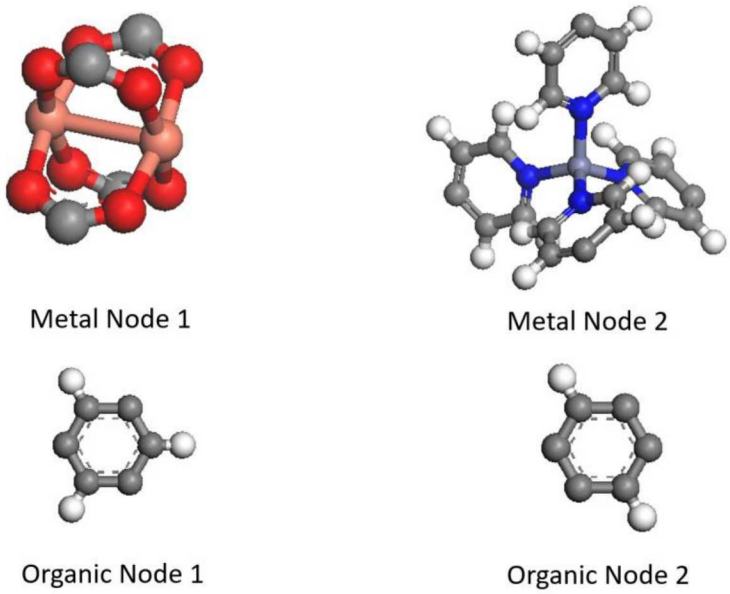

Figure 1: Building blocks used to construct the MOF nodes used in this study. Metal Node 1 is a Cu-paddlewheel node ($Cu_2(COO)_4$). Here we show the carboxylic acids, which are usually considered part of the organic linker, to indicate the four connection points. All of the MOFs in this work that contain Metal Node 1 have four connections, meaning they also have unsaturated metal sites on the node. Metal Node 2 is a Zn-based node ($ZnN_4(C_5H_4)_4$. The two organic nodes are both based on phenyl rings. Organic Node 1 has 3 connections to the ditopic edges on alternating carbons. Organic Node 2 has 4 connections to edges. Color key: Cu (orange), Zn (purple), O (red), C (gray), H (white).

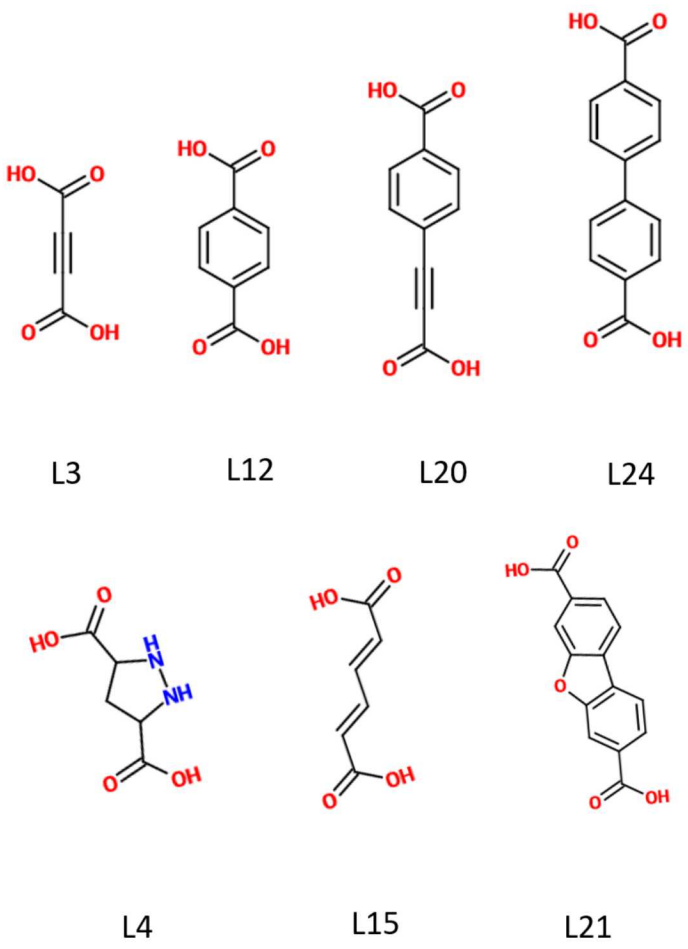

Figure 2: Organic edges used to construct the MOFs in this work. Naming scheme retained from the original paper by Colón and Gómez-Gualdrón.[28]

2.2 Monte Carlo Simulations

Monte Carlo simulations were performed using the multipurpose molecular simulation code RASPA.[32] Following the methodology previously described by Chung et al.[20], we used Lennard-Jones parameters taken from the Universal force field (UFF)[30] for the MOF framework atoms and the TraPPE united-atom force field[33] for the adsorbates. Framework atoms were held fixed at their crystallographic coordinates. The MOF−adsorbate interactions were treated using a cutoff of 12.8 Å with no tail corrections. The adsorbate-adsorbate interactions were treated using a 14.0 Å cutoff with tail corrections, which is specified as part of the TraPPE force field. The implementation of two cutoffs was achieved by using pre-tabulated grids for the adsorbate−MOF potential energy and specifying the TraPPE cutoff for adsorbate-adsorbate interactions during the simulation. The grids were computed using a 0.1 Å spacing. No partial charges were assigned to the MOF framework atoms or the adsorbate (united) atoms.

Henry constant calculations were done using Widom insertions in RASPA using 100,000 cycles and configurational biasing for each adsorbate. The grand canonical Monte Carlo (GCMC) simulations used a total of 100,000 cycles (50,000 initialization cycles and 50,000 production cycles) for single component adsorption and 200,000 cycles (100,000 initialization and 100,000 production cycles) for multicomponent adsorption. All GCMC simulations used configurational biasing for the adsorbates. The simulation box was chosen to be sufficiently large to exceed twice the Lennard-Jones cutoff in each dimension.

Textural properties such as the pore size distribution and surface area were calculated using Zeo++ (v 0.2.2).[34-35] Surface area and pore size calculations were done using a nitrogen probe with a radius of 1.8 Å. Vapor pressures for the adsorbates were computed using the Antoine equation with parameters taken from the NIST Webbook.[36]

2.3 DFT Calculations for Structural Optimizations

The unit cells (i.e. atomic positions, lattice constants, and unit cell shape) of selected MOFs were optimized using periodic DFT as implemented in the Vienna *ab initio* Simulation Package (VASP) 5.4.1.[37-38] The PBE-D3(BJ) level of theory[39-41] was used with v.5.4 of the VASP-recommended projector-augmented wave (PAW) pseudopotentials.[42] This level of theory has been shown to accurately reproduce the geometries of several MOFs.[43-44] Using the workflow described and benchmarked in prior work,[45] a plane-wave kinetic energy cutoff of 520 eV was applied, and all calculations were carried out with a k-point density of approximately 1000/number of atoms per cell (as determined with Pymatgen[46]). This corresponds to the Γ-point only for all the MOFs. Each structure was optimized until a maximum force tolerance of 0.03 eV/Å was achieved. To ensure accurate forces, each self-consistent field (SCF) loop was converged to within 10^{-6} eV. The conjugate gradient algorithm was used to carry out the geometry optimizations, the preconditioned conjugate gradient "all bands simultaneous update of orbitals" algorithm was used to converge the SCF[47-50], and the accurate precision keyword was enabled in VASP. Symmetry operations were disabled. Gaussian smearing of the band occupancies with a smearing width of 0.01 eV was applied with extrapolation back to the 0 K limit. Spin-polarization was considered for all calculations with each of the two Cu(II) species in each paddlewheel unit antiferromagnetically aligned, corresponding to the open-shell singlet state. This is consistent with several prior studies that have shown Cu-BTC exhibits antiferromagnetic coupling between the Cu(II) sites within a given node.[51-54]

2.4 Selectivity

For the multicomponent simulations, we defined the adsorption selectivity for a given isomer using a variant of the conventional definition for selectivity of binary mixtures, where component i is the desired isomer and component j is defined as the sum of all other isomers:

$$S_i = \frac{x_i y_j}{y_i x_j} \qquad \text{Eq. 1}$$

Here x_i and y_i are the mole fractions of component i in the adsorbed and gas phases, respectively.

3: Results and Discussion

3.1 Initial Screening

In order to quickly identify the most interesting sets of MOFs from our set of 38 structures, we computed the Henry's constants and the heats of adsorption using Widom insertions for all alkane isomers ranging from 1−6 carbons in all 38 MOFs. The alkanes used in this work are methane, ethane, propane, *n*-butane, isobutane, *n*-pentane, 2-methylbutane, neopentane, *n*-hexane, 2-methylpentane, 3-methylpentane, 2,3-dimethylbutane, and 2,2-dimethylbutane. The data for the C1-C4 molecules are shown in the Supplemental Information in Supplemental Table 2 and Supplemental Table 3, and the Henry's constant data for the C5 and C6 isomers are shown in Supplemental Table 4 and Supplemental Table 5. Henry's constants for the C5 and C6 isomers in selected MOFs are shown in Table 1.

The Henry's constants for the MOF nbo_L12 (Table 1) stand out due to the high values for the linear isomers, particularly compared to their branched counterparts. In nbo_L12 at 300 K, the Henry's constants for n-pentane and n-hexane are 0.42 and 6.3 mol/kg/Pa, respectively, while the values for the branched C5 isomers are around 10^{-4} mol/kg/Pa and the values for the branched C6 isomers are around 10^{-3} mol/kg/Pa. Therefore, the Henry's constants for the linear isomers are about 1000 times higher than the branched isomers in nbo_L12. This indicates there is a high selectivity for the linear isomers, which is a useful property in the context of industrial separations, which often seek to isolate linear alkanes to recycle to an isomerization process.

We see a similar trend in the heats of adsorption shown in Table 2. The computed heat of adsorption for n-pentane in nbo_L12 at 300 K is −52.7 kJ/mol, compared to −18.7 kJ/mol for 2-methylbutane and −12.5 kJ/mol for neopentane. This difference in the heats of adsorption between linear and branched isomers (34−40 kJ/mol) is much larger than the difference seen for any of the other MOFs in this data set. In most of the other structures, the heat of adsorption for 2-methylbutane is within 3 kJ/mol of n-pentane, and in 30 of the 38 MOFs they are within 1 kJ/mol. Many of the MOFs have similar heats of adsorption for n-pentane and neopentane as well. However, neopentane does have a larger difference from n-pentane in some MOFs with small pores (e.g. 14.5 kJ/mol in rhr_L3 and 10.5 kJ/mol in ssb_L15) because it is a bulky molecule, which is not favored in the narrow pores in those structures.

The MOF rhr_L12 also stands out due to its moderate selectivity for the branched isomers. Most MOFs in Table 2 display little or no selectivity for the branched isomers 2-methylbutane and neopentane. However, rhr_L12 favors 2-methybutane over pentane by 4.6 kJ/mol and neopentane over pentane by 3.2 kJ/mol which is the highest selectivity for either branched isomer. This is especially interesting because rhr_L12 and nbo_L12 are polymorphs. There is a third MOF, lvt_L12, which is also a polymorph

with these two materials. lvt_L12 does not show significant linear/branched selectivity based on the Henry's constants and heats of adsorption.

This polymorph family is a good example of how the choice of topology can influence the adsorption properties and selectivity of the MOF. These three polymorphic MOFs, nbo_L12, rhr_L12, and lvt_L12, have the same nodes and linkers and the same chemical formula, but one is slightly selective for branched isomers and one is highly selective for linear isomers based solely on their different topology and pore structure. Due to the unique properties of this particular polymorph family we will discuss these three MOFs in more depth.

Table 1: Henry's constants for alkanes in 3 selected MOFs at 300 K. Values are in units of mol/kg/Pa.

MOF	*n*-pentane	neopentane	2-methylbutane	*n*-hexane	2-methylpentane	3-methylpentane	2,2-dimethylbutane	2,3-dimethylbutane
lvt_L_12	2.5E-02	9.1E-03	3.0E-02	1.6E-01	1.9E-01	2.4E-01	2.0E-01	3.1E-01
nbo_L_12	4.2E-01	2.1E-04	7.9E-04	6.3E+00	4.5E-03	3.2E-03	1.4E-03	2.3E-03
rhr_L_12	4.8E-03	6.2E-03	1.2E-02	1.8E-02	3.2E-02	4.3E-02	9.2E-02	9.4E-02

Table 2: Heats of adsorption in kJ/mol for C5 alkanes computed from Widom insertions at 300 K. The two columns on the far right indicate the respective difference in heat of adsorption from 2-methylbutane and neopentane with that of pentane. The row containing nbo_L12 is bolded for emphasis. Sorted by topology

MOF	pentane	2-methylbutane	neopentane	[pentane − 2-methylbutane]	[pentane − neopentane]
dia_L12	-7.1	-6.4	-3.2	-0.7	-3.9
dia_L20	-4.7	-4.2	-1.1	-0.5	-3.6
dia_L24	-6.1	-5.5	-2.1	-0.6	-4.0
dia_L3	-4.1	-4.0	-1.4	-0.1	-2.7
lcs_L12	-8.2	-7.7	-4.2	-0.5	-4.0
lcs_L20	-5.0	-4.5	-1.4	-0.5	-3.6
lcs_L24	-6.3	-5.7	-2.3	-0.6	-4.1
lcs_L3	-5.0	-4.8	-2.1	-0.3	-2.9
lvt_L12	-23.4	-24.8	-21.8	1.4	-1.6
lvt_L20	-13.6	-13.5	-10.6	-0.1	-3.0
lvt_L24	-10.0	-10.6	-7.9	0.6	-2.1
lvt_L3	-19.8	-20.6	-18.0	0.9	-1.7
nbo_L12	**-52.7**	**-18.7**	**-12.5**	**-34.0**	**-40.2**
nbo_L20	-6.5	-6.7	-3.8	0.2	-2.8
nbo_L24	-10.2	-10.3	-7.3	0.2	-2.8
nbo_L3	-6.2	-6.7	-4.9	0.6	-1.3
pto_L12	-12.1	-13.3	-10.3	1.2	-1.8
pto_L20	-6.5	-6.7	-3.7	0.2	-2.8
pto_L24	-8.0	-8.0	-4.5	0.0	-3.4
pto_L3	-7.2	-7.6	-5.6	0.5	-1.6
rhr_L12	-24.3	-28.8	-27.5	4.6	3.2
rhr_L20	-10.1	-10.1	-6.9	0.1	-3.1
rhr_L24	-12.9	-13.0	-9.7	0.1	-3.2
rhr_L3	-16.1	-8.8	-1.6	-7.3	-14.5
sod_L12	-7.0	-6.4	-3.1	-0.6	-3.9
sod_L20	-5.1	-4.6	-1.2	-0.5	-3.8
sod_L24	-6.8	-6.1	-2.4	-0.7	-4.4
sod_L3	-5.5	-5.3	-2.5	-0.2	-3.0
ssa_L15	-23.4	-22.3	-17.1	-1.1	-6.4
ssa_L21	-24.9	-25.5	-19.7	0.7	-5.2
ssa_L4	-34.1	-32.3	-24.1	-1.8	-10.0
ssb_L15	-21.7	-18.9	-11.1	-2.8	-10.5
ssb_L21	-20.7	-21.5	-17.0	0.8	-3.7
ssb_L4	-16.5	-17.0	-13.7	0.5	-2.9
tbo_L12	-13.2	-13.1	-9.5	-0.1	-3.7
tbo_L20	-6.7	-6.8	-3.7	0.1	-3.0
tbo_L24	-9.4	-9.9	-6.6	0.5	-2.7
tbo_L3	-11.1	-11.8	-9.3	0.7	-1.7

3.2 Textural Properties of Selected MOFs

Despite being made from exactly the same nodes and linkers, these three MOFs have very different pore sizes and configurations, as seen in Figure 3. The textural properties are summarized in Table 3 and the pore size distributions are shown in Supplemental Figure 2.

As shown in Figure 3, nbo_L12 has a hierarchical pore structure consisting of small triangular pores (4.9 Å) and larger hexagonal pores (14.0 Å) that form 1D channels. The rhr_L12 MOF has a large nearly spherical pore (28.2 Å) with square and hexagonal windows leading into the pore, similar to how the surface of a soccer ball is made of hexagonal and pentagonal patches. lvt_L12 has two slightly different pore sizes: 8.0 and 8.6 Å. As seen in Figure 3, lvt_L12 has a pore structure consisting of 1D square channels with Cu paddlewheel nodes in the vertices. The different pore sizes in lvt_L12 arise from the fact that the Cu paddlewheel nodes are not all aligned parallel to one other. Instead, they form a zig-zag pattern that results in alternating channels of slightly different size.

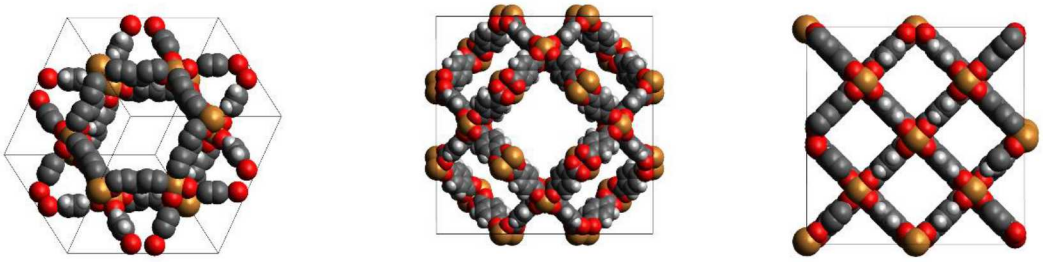

nbo_L12 rhr_L12 lvt_L12

Figure 3: Visualization of the three selected MOFs: nbo_L12, rhr_L12, and lvt_L12. These three MOFs are polymorphs. The grey spheres are C, red is O, orange is Cu, and white is H.

Table 3: Summary of textural properties for three selected polymorphs. VF indicates the void fraction. The pore size is taken from the peaks in the pore size distribution shown in Supplemental Figure 2.

	VF	Density	Surface Area		Pore size (Å)
MOF		**g/cm³**	**m²/cm³**	**m²/g**	
nbo_L12	0.66	0.84	1077	1286	4.9, 14.0
rhr_L12	0.88	0.37	1480	4046	28.2
lvt_L12	0.70	0.82	1500	1821	8.0, 8.6

Table 4: Dimensions and kinetic diameters of C6 alkane isomers. X, Y, and Z indicate the length of the molecule along the three directions, and the final column is the kinetic diameter for the molecule. All values are in angstroms.

Alkane	X	Y	Z	Kinetic Diameter
n-hexane	9.7	4.5	4	4.3
2-methylpentane	9.2	6.2	5.2	5
3-methylpentane	9.3	6.2	5.2	5
2,2-dimethylbutane	8	6.7	5.9	6.2
2,3-dimethylbutane	7.8	6.7	5.3	5.6

Table 4 shows the dimensions and kinetic diameters[55] for the C6 alkane isomers. Comparing the sizes of these molecules to the pore sizes of the MOFs reported in Table 3, we surmise that nbo_L12 has the potential to separate the linear and branched isomers based on size. *n*-Hexane has a kinetic diameter of 4.3 Å, which is less than the width of the small triangular pore in nbo_L12 (4.9 Å), while the dimethylbutanes are too large. We will discuss the implications of this further in the following sections. Note in this work, we are considering equilibrium adsorption, not diffusion; therefore, we are not focused on transport limitations that might be caused by the window size, so long as the windows are large enough for molecules to fit into the pores.

3.3 Single Component Adsorption

We computed adsorption isotherms for each C5 and C6 alkane in the three selected MOFs of interest: nbo_L12, rhr_L12, and lvt_L12. The isotherms are shown in Figure 4. We observe similar trends between the C5 and C6 isomers. In nbo_L12 (Figure 4a), the linear isomer is preferentially adsorbed at low pressure, consistent with our predictions from the Henry's constants in Table 1 and heats of adsorption in Table 2. For both the C5 and C6 groups, the monobranched isomers (2-methybutane, 2-methylpentane, and 3-methylpentane) reach saturation at about the same loading as their respective linear isomers, pentane and hexane, while the dibranched isomers (neopentane, 2,2-dimethylbutane, and 2,3-dimethylbutane) are saturated at lower uptake. This suggests that the bulkier dibranched isomers cannot access the smaller pores in nbo_L12 which can accommodate the linear and monobranched isomers. Therefore, nbo_L12 could be of interest for size-based separation applications. The linear isomer is the most preferred, but the monobranched isomers can fit into the small pores. The bulkier neopentane and dimethylbutanes cannot fit into the small triangular pores even at high pressure.

This adsorption behavior is confirmed by examining snapshots of the GCMC simulations, shown in Figure 5. All calculations shown in Figure 5 were done at 300 K. In nbo_L12 at low pressure (10 Pa, Figure 5a),

n-hexane almost exclusively goes into the small triangular pores. As the pressure increases and these pores are filled, *n*-hexane begins to fill the large hexagonal pores (1000 Pa, Figure 5b). At low pressure, 2-methylpentane prefers to stay in the large pores (100 Pa, Figure 5c); however, at high pressure it can be forced into the small pores (1000 Pa, Figure 5d). 2,3-dimethylbutane cannot squeeze into the small triangular pores even at high pressure because it is simply too large (1000 Pa, Figure 5e and 10,000 Pa, Figure 5f).

In rhr_L12 (Figure 4c), we see that the uptake of all the alkanes is fairly low until the pressure reaches about 0.1 P/P_0, and then the pores quickly become saturated. Since the rhr_L12 pores are so large (28.2 Å) there is no size exclusion among the isomers, and all of the C6 isomers reach saturation at about 17 mol/kg. Overall, due to the very large pores in rhr_L12 this MOF has little selectivity for C6 isomers. For the C5 isomers, pentane and 2-methylbutane reach saturation at about 19 mol/kg at $P = P_0$. Neopentane appears to have not reached saturation at $P = P_0$, and the uptake is lower than *n*-pentane at 14.8 mol/kg. This is likely due to the bulky, nearly spherical nature of neopentane, which has a kinetic diameter of 6.2 Å (compared to 4.3 Å for *n*-pentane), and therefore cannot pack as efficiently in the pores as *n*-pentane and 2-methylbutane (5.0 Å). [56]

We see more pronounced effects of packing at the saturation pressure in lvt_L12. In Figure 4b, the saturation capacity clearly decreases as the isomers become more branched. The linear isomer has a saturation capacity of 5.2 mol/kg, while 3-methylpentane is 4.5 mol/kg and the bulkiest isomer (2,2-dimethylbutane) has a saturation capacity of 3.5 mol/kg. The pores in lvt_L12 are 8−8.6 Å, which is close to twice the kinetic diameter of the linear alkane, suggesting that two linear molecules (or the linear portions of methylpentane) could potentially sit adjacent to each other in a pore if they are aligned in just the right arrangement. However, the kinetic diameter of 2,2-dimethylbutane is 6.2 Å such that only one molecule can fit into a pore, leaving some unoccupied space around it. This inefficient packing accounts for the decrease in capacity with adsorbate branching in the lvt_L12 MOF.

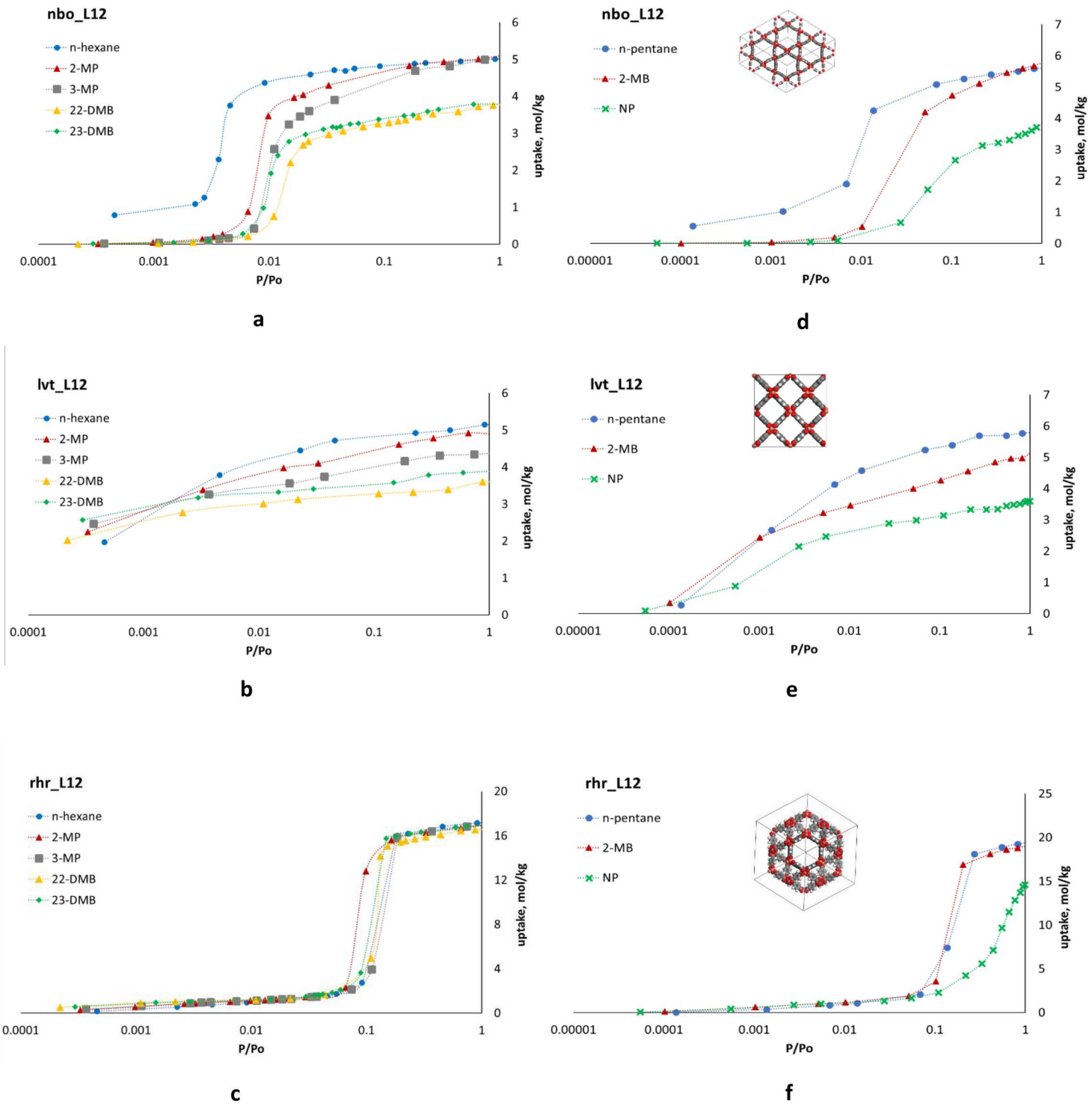

Figure 4: Single component adsorption isotherms at 300 K for C6 alkanes in a) nbo_L12, b) lvt_L12, and c) rhr_L12 and C5 alkanes in d) nbo_L12, e) lvt_L12, and f) rhr_L12. The adsorbate names are abbreviated as 2-MB for 2-methylbutane, NP for neopentane, 2-MP for 2-methylpentane, 3-MP for 3-methylpentane, 22-DMB for 2,2-dimethylbutane, and 23-DMB for 2,3-dimethylbutane. The insets in d,e, and f show visualizations of the respective MOF structures. Computed vapor pressures are shown in Supplemental Table 7.

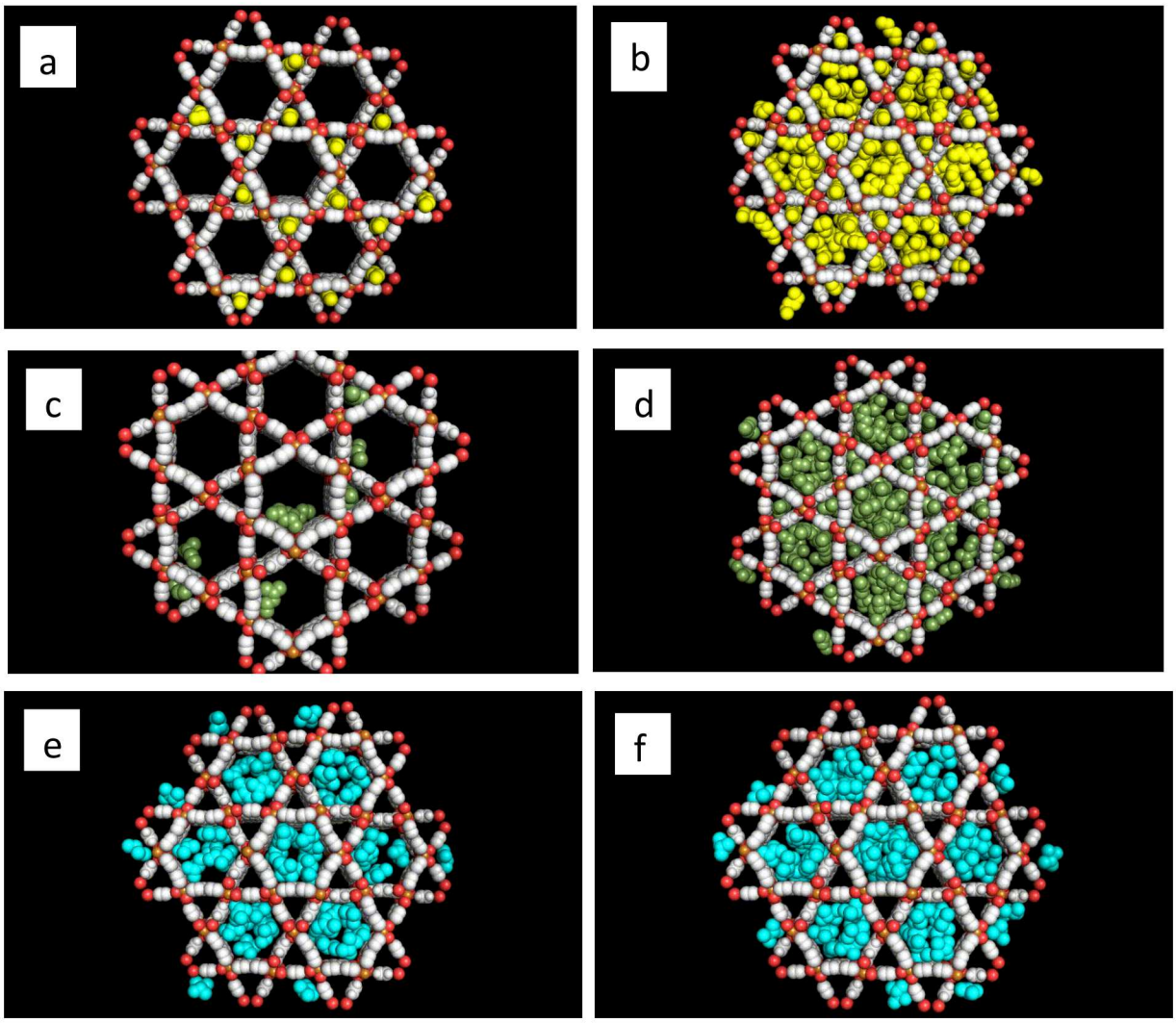

Figure 5: Snapshots of GCMC simulations of C6 isomers in nbo_L12 MOF at 300 K and various pressures. a) n-hexane, 10 Pa, b) n-hexane, 1000 Pa, c) 2-methylpentane, 100 Pa, d)2-methylpentane, 1000 Pa, e)2,3-dimethylbutane, 1000 Pa, and f) 2,3-dimehtylbutane, 10000 Pa. Yellow molecules are n-hexane, green molecules are 2-methylpentane, and light blue molecules are 2,3-dimethylbutane. The white atoms in the framework are C, the orange framework atoms are Cu, and the red framework atoms are O.

3.4 Thermodynamic Analysis of Adsorption

We can gain more insight into the selectivity of the three MOFs by analyzing the thermodynamics of adsorption. The Helmholtz free energy of adsorption (ΔA_{ads}), enthalpy of adsorption (ΔH_{ads}), and entropy of adsorption ($-T\Delta S_{\mathrm{ads}}$) at infinite dilution at 300 K are shown in Table 5. It is clear that the adsorption of the linear C4, C5, and C6 isomers is highly favored enthalpically in nbo_L12, owing to the strong attraction inside the small pores. The enthalpy of adsorption for *n*-butane in nbo_L12 is −54.0 kJ/mol compared to −24.1 kJ/mol for isobutane, and the enthalpy of adsorption for *n*-hexane is −77.6 kJ/mol compared to −29.9 kJ/mol for 2,2-dimethylbutane. However, due to the tight fit of the linear isomers in the small pore, the configurations the molecules can adopt are greatly restricted. This results in a large entropic penalty: 39.1 kJ/mol for *n*-hexane and 29.0 kJ/mol for *n*-butane. At 300 K, the difference in enthalpy between the linear and branched isomers outweighs the entropic term, so the free energy indicates that the adsorption is selective for the linear isomers. For the C6 isomers, the free energy indicates that adsorption of *n*-hexane is favored by 18−20 kJ/mol over any of the branched isomers. At 433 K, this difference is reduced to 9−10 kJ/mol in nbo_L12, but the linear isomer is still favored. Data for 433 K are shown in Supplemental Table 6.

The Helmholtz free energy indicates very slight selectivity for the branched C6 isomers in lvt_L12, with a difference of only 1.6 kJ/mol between *n*-hexane and 2,3-dimethylbutane at 300 K. *n*-Butane and isobutane have exactly the same free energy (−22.1 kJ/mol). The small thermodynamic selectivity at infinite dilution reinforces our conclusion that the differences in saturation loadings for the isomers seen in Figure 4 for lvt_L12 are the result of packing effects at high loading.

rhr_L12 is slightly selective for the branched isomers based on the Helmholtz free energy. The enthalpic selectivity is more pronounced but partially offset by the large entropic penalty for the adsorption of the branched isomers. This is opposite of the trend seen in nbo_L12 where the linear isomers experience a larger entropic penalty for adsorption. In rhr_L12 at 300 K, the difference in enthalpy of adsorption for *n*-hexane and 2,3-dimethylbutane is 6.6 kJ/mol, while the difference in free energy is only 4.2 kJ/mol due to the difference in the entropy of adsorption. Therefore, the slight selectivity for branched isomers we observe in rhr_L12 at low pressure is driven by enthalpy. At low pressure, the adsorbate molecules prefer to lie in the windows of the rhr_L12 MOF rather than the middle of the large pore (Supplemental Figure 3). This arrangement provides stronger enthalpic interactions for the branched molecules, but also more entropic restriction. At higher pressure the windows are filled, and the molecules go into the middle of the pore where there is no significant selectivity from the MOF, as shown in Supplemental Figure 3.

Table 5: Thermodynamic properties for the adsorption of alkanes at 300 K and infinite dilution.

300 K	ΔA_{ads} (kJ/mol)			ΔH_{ads} (kJ/mol)			$-T\Delta S_{ads}$ (kJ/mol)		
	nbo_L12	rhr_L12	lvt_L12	nbo_L12	rhr_L12	lvt_L12	nbo_L12	rhr_L12	lvt_L12
methane	-8.7	-3.7	-6.7	-18.2	-7.8	-11.1	12.0	6.6	6.9
ethane	-15.9	-8.2	-12.0	-31.1	-16.7	-17.5	17.7	11.1	8.1
propane	-20.7	-13.3	-17.0	-41.6	-25.8	-23.7	23.3	15.0	9.2
***n*-butane**	-27.5	-17.7	-22.1	-54.0	-32.2	-30.0	29.0	17.0	10.4
isobutane	-14.9	-19.1	-22.1	-24.1	-34.5	-29.9	11.7	17.9	10.3
***n*-pentane**	-34.1	-21.0	-27.0	-65.4	-37.0	-36.1	33.8	18.5	11.6
neopentane	-15.2	-21.6	-24.5	-23.7	-38.7	-33.0	11.0	19.6	10.9
2-methylbutane	-18.5	-23.2	-27.6	-30.5	-40.7	-36.7	14.5	19.9	11.6
***n*-hexane**	-41.1	-24.2	-31.7	-77.6	-41.6	-42.6	39.1	19.9	13.4
2-methylpentane	-22.6	-25.6	-32.1	-39.4	-44.6	-42.7	19.3	21.4	13.0
3-methylpentane	-22.0	-26.4	-32.7	-35.9	-45.6	-42.9	16.4	21.8	12.7
2,2-dimethylbutane	-20.0	-28.2	-32.2	-29.9	-47.7	-42.1	12.4	22.0	12.4
2,3-dimethylbutane	-21.1	-28.4	-33.3	-31.8	-48.2	-43.5	13.2	22.3	12.7

3.5 Multi-component Adsorption

We computed adsorption isotherms for equimolar mixtures of C6 isomers at an elevated temperature of 433 K, which more closely resembles the conditions of an industrial separation process, for nbo_L12, rhr_L12, and lvt_L12. The computed isotherms are shown in Figure 6. As expected, nbo_L12 shows high selectivity for the linear hexane isomer over the range of pressures from 0 to 1 bar (Figure 6a). Similarly, nbo_L12 selectively adsorbs n-pentane over 2-methylbutane and neopentane; at 433 K and 1 bar, nbo_L12 adsorbs 1.3 mol/kg of n-pentane compared to 0.56 mol/kg 2-methylbutane and 0.24 mol/kg neopentane (Supplemental Table 8).

rhr_L12 displays some moderate selectivity for the dimethylbutanes at 433 K and 1 bar (Figure 6b), consistent with the slightly more favorable Henry's constants and free energy of adsorption we computed for the branched isomers in rhr_L12.

lvt_L12 is also selective for the branched isotherms (Figure 6c). At 433 K and 1 bar, the ranking of isomer adsorption in lvt_L12 is 2,3-dimethylbutane > 3-methylpentane > 2-methylpentane ≈ 2,2-dimethylbutane > *n*-hexane. This also mirrors the computed free energy of adsorption shown in Supplemental Table 6. This selectivity for branched isomers is opposite to what we might have expected based on the single-component isotherms which showed higher saturation loading for the linear isomer hexane. However, the separation seen at the saturation loading for the pure components is based on geometric factors like the packing of the molecules in the pores. The smaller, linear molecules can be packed more efficiently in the pores, but in a mixture, they are outcompeted thermodynamically by the

branched molecules. The adsorption of 2,3-dimethylbutane is 2.0 kJ/mol more favorable than *n*-hexane based on free energy (Supplemental Table 6), so it is adsorbed preferentially out of the mixture.

The different behaviors shown in Figure 6 demonstrate how the choice of topology can greatly influence the adsorption behavior and even invert the selectivity. The adsorption isotherms in Figure 6 represent an equimolar solution, but in reality, the feed for an industrial separation process might vary in its composition significantly. It is important that a sorbent exhibit the desired selectivity over the full spectrum of feed compositions that might be relevant. In order to test the robustness of the high selectivity of nbo_L12 with varying composition, we computed the adsorption and selectivity for the C6 alkanes over a wide range of compositions with the mole fraction of each component ranging from 10−60% in 10% increments. The relationship between selectivity and the feed composition for nbo_L12 at 1 bar and 433 K is shown in Figure 7.

In nbo_L12 the selectivity for *n*-hexane is about 3.8−4.4 when the feed fraction of *n*-hexane is 0.1, and the selectivity drops to about 2 when the feed fraction of *n*-hexane is 0.6. The selectivity for all the other isomers remains below 1.0 at all compositions. This decrease in hexane selectivity is the result of the small triangular pores, which drive the selective adsorption of the normal isomer, becoming saturated. Once the highly selective small pores are full, *n*-hexane is adsorbed in the large hexagonal pore, which does not differentiate strongly between the isomers. This drives down the overall selectivity as the fraction of *n*-hexane in the feed increases because the denominator of Eq. 1 increases while the amount of n-hexane adsorbed in the small pores remains constant, and the large hexagonal pores are not strongly selective. For both lvt_L12 and rhr_L12, the general trend in selectivity does not change much at different feed compositions as shown in Supplemental Figure 4.

Table 6a shows the composition of the adsorbed phase in each type of pore in nbo_L12. These results are averages based on configurations from GCMC simulations at 433 K and 1 bar using an equimolar gas phase mixture. Separate simulations were done for the C5 alkanes and the C6 alkanes. The data in Table 6a show that the small triangular pore contains more than 99% pure pentane or hexane across a range of pressures. At 0.01 bar for both alkanes the small pore contains only the linear isomer. At 0.1 bar and 1.0 bar, trace amounts of methylpentane molecules are found in the triangular pore, but the pore overall still contains over 99% *n*-hexane. Neopentane and dimethylbutane are never found in the small pore at any pressure.

Table 6b shows the percentage of the total molecules of a given isomer that reside in each pore. For example, for *n*-pentane at 1.0 bar, 48.0% of the *n*-pentane molecules are found in the triangular pore and 52.0% are found in the hexagonal pore. However, looking back at Table 6a, we know that the molecules found in the small triangular pore are 99.8% *n*-pentane and 0.2% 2-methylbutane. At 1.0 bar, 99.6% of the adsorbed 2-methylpentanes are in the large hexagonal pore, and only 0.4% are in the triangular pore. This shows that even though it is possible for the methylpentane and 2-methylbutane to fit into this small pore, it is much more favorable for the linear isomers to adsorb there, and even at high pressure the composition of the small pores remains almost entirely *n*-pentane or *n*-hexane.

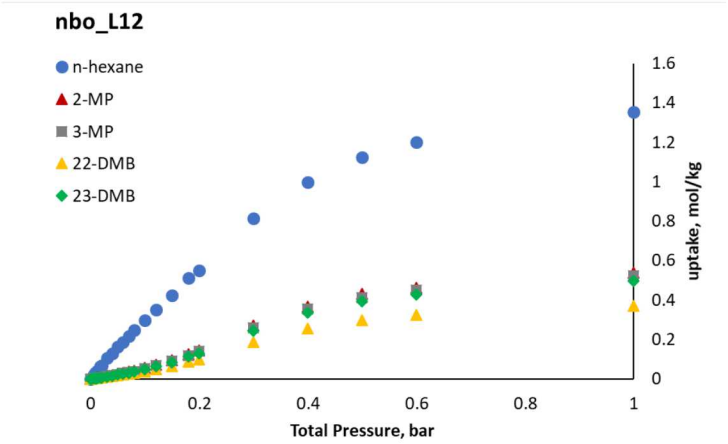

a

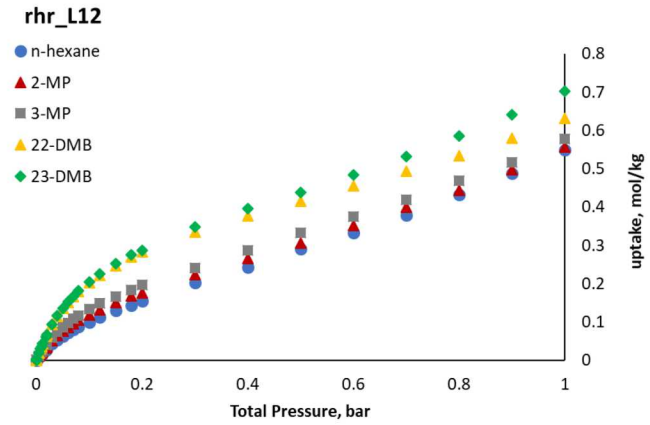

b

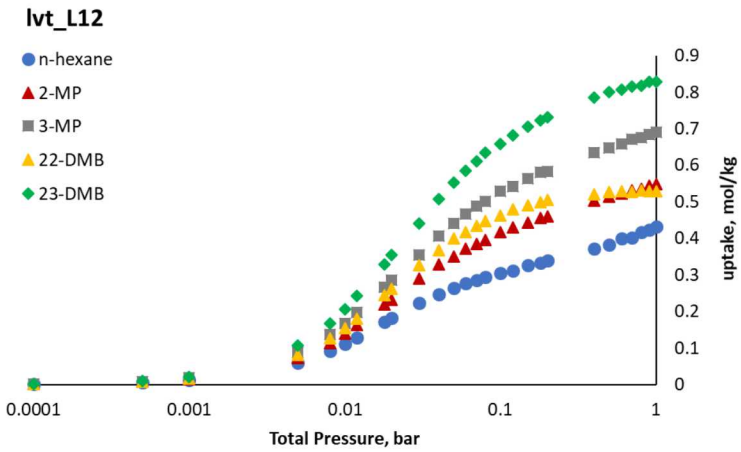

c

Figure 6: Simulated adsorption isotherms for C6 alkanes at 433 K in a) nbo_L12, b) rhr_L12, c) lvt_l12. These isotherms are based on equimolar gas-phase mixtures of the isomers. The adsorbate names are abbreviated as 2-MP for 2-methylpentane, 3-MP for 3-methylpentane, 22-DMB for 2,2-dimethylbutane, and 23-DMB for 2,3-dimethylbutane.

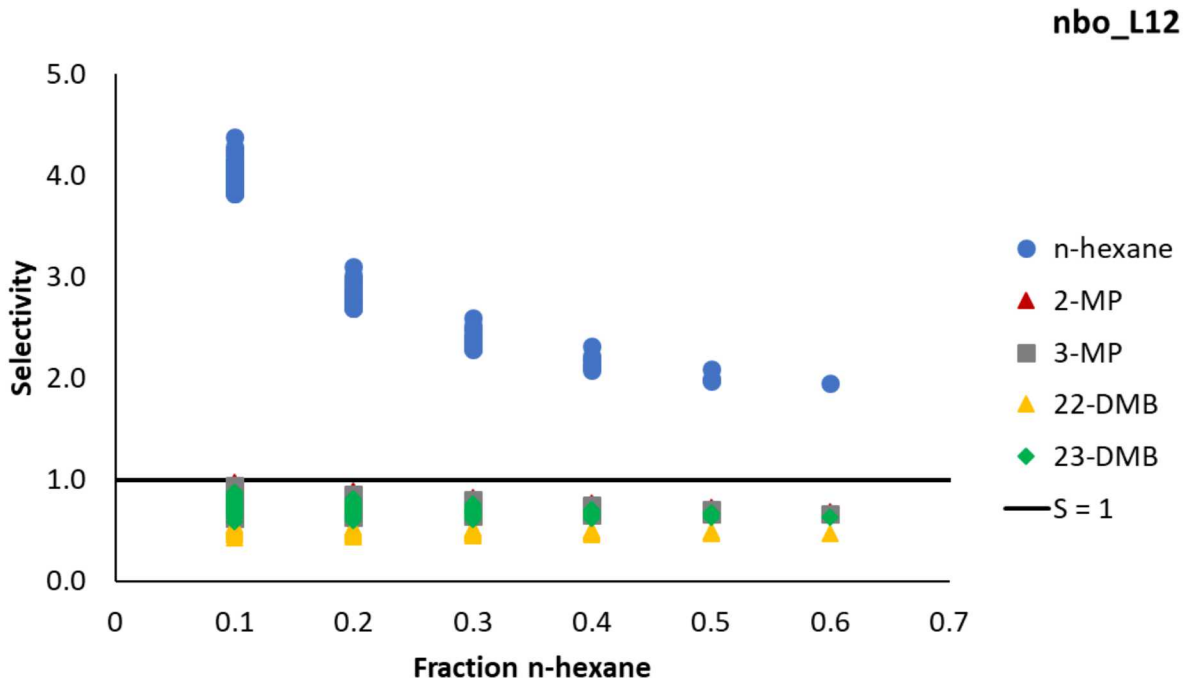

Figure 7: Selectivity vs. gas-phase molar composition for C6 alkanes in nbo_L12 at 433 K and 1 bar. The horizontal axis represents the mole fraction of n-hexane in the gas phase mixture. The vertical axis is the selectivity of the adsorbed phase for the different components. Note that there are multiple points at each value on the horizontal axis because the mole fraction of the other components can change at a constant fraction of n-hexane. The black line indicates a selectivity (S) equal to one. The adsorbate names are abbreviated as 2-MP for 2-methylpentane, 3-MP for 3-methylpentane, 22-DMB for 2,2-dimethylbutane, and 23-DMB for 2,3-dimethylbutane.

Table 6: Type of molecules that reside in the different shaped pores of nbo_L12, based on random configurations from GCMC simulations at 433 K and 1 bar with an equimolar gas phase. a) The composition of the molecules inside the triangle pore and the composition of the molecules in the hexagonal pore, b) The percentage of the total number of each type of adsorbed molecule that lies in the triangular pore or the hexagonal pore

a

1 bar	composition in triangles (%)			composition in hexagons (%)		
433 K	**0.01 bar**	**0.1 bar**	**1.0 bar**	**0.01 bar**	**0.1 bar**	**1.0 bar**
***n*-pentane**	100.0	100.0	99.8	49.9	44.2	46.0
2-methylbutane	0.0	0.0	0.2	0.0	32.6	38.7
neopentane	0.0	0.0	0.0	50.1	23.3	15.3
***n*-hexane**	100.0	99.2	99.6	35.1	23.7	25.3
2-methylpentane	0.0	0.4	0.3	25.0	19.4	20.5
3-methylpentane	0.0	0.4	0.1	10.0	20.9	19.6
2,2-dimethylbutane	0.0	0.0	0.0	10.0	16.2	14.8
2,3-dimethylbutane	0.0	0.0	0.0	20.0	19.8	19.7

b

1 bar	% in triangles			% in hexagons		
433 K	**0.01 bar**	**0.1 bar**	**1.0 bar**	**0.01 bar**	**0.1 bar**	**1.0 bar**
***n*-pentane**	81.3	79.9	48.0	18.7	20.1	52.0
2-methylbutane	0.0	0.0	0.2	100.0	100.0	99.8
neopentane	0.0	0.0	0.0	100.0	100.0	100.0
***n*-hexane**	86.5	79.6	54.6	13.5	20.4	45.4
2-methylpentane	0.0	1.8	0.4	100.0	98.2	99.6
3-methylpentane	0.0	1.7	0.2	100.0	98.3	99.8
2,2-dimethylbutane	0.0	0.0	0.0	100.0	100.0	100.0
2,3-dimethylbutane	0.0	0.0	0.0	100.0	100.0	100.0

3.6 Topological Structure of nbo_L12

The structure of nbo_L12 is an interesting case among **nbo** MOFs. The **nbo** topology is comprised of alternating four-connected building blocks, as seen in the prototypical **nbo** MOF-505.[57] There is some variation based on the size of the building blocks and the angles of rotation between them, but often the **nbo** topology yields MOFs with cubic pores and identical structure in the [001], [010], and [100] directions, as seen in Figure 8a. However, nbo_L12 has 1D channels made of triangles and hexagons arranged in a Kagome lattice. Similar patterns have been reported in **nbo** MOFs before: Chun et al.[58]

have reported a Cu and pyrimidine-5-carboxylate MOF [$Cu(pmc)_2$] that has a similar 1D trihexagonal pore structure as we see in nbo_L12; however, in [$Cu(pmc)_2$] the pore structure is the result of interpenetrating nets. The MOF is made of two independent but isomeric nets, and the authors ascribe the structure to inter-net interactions between the Cu and N atoms on each net.

Zaworotko et al.[59] reported that 5-(*N*-phthalimide)isophthalic acid could form either an **nbo** topology or a Kagome lattice when reacted with $CuCl_2$ depending on the choice of solvent. However, in that work the Kagome lattice is made of 2D layers held together by π-π stacking between the aromatic linkers. The sheets are not connected by any bonds. The Kagome lattice is not the same crystal structure as the **nbo** MOF, although they contain the same building blocks. In this case, the **nbo** MOF cannot be converted into the Kagome lattice without rearranging bonds because they are distinct structures.

nbo_L12 is different from these two cases. It is made of a single net with no interpenetration, and the layers along the 1D channels are connected, giving it a helical structure. nbo_L12 can "unfold" from the 1D triangle channel structure (called here the "star conformation", Figure 8b) to the cubic conformation (Figure 8a) *without breaking any bonds or forming any new bonds.* The connectivity networks of the two conformations are identical. Additional visualizations of nbo_L12 are shown in Supplemental Figure 5.

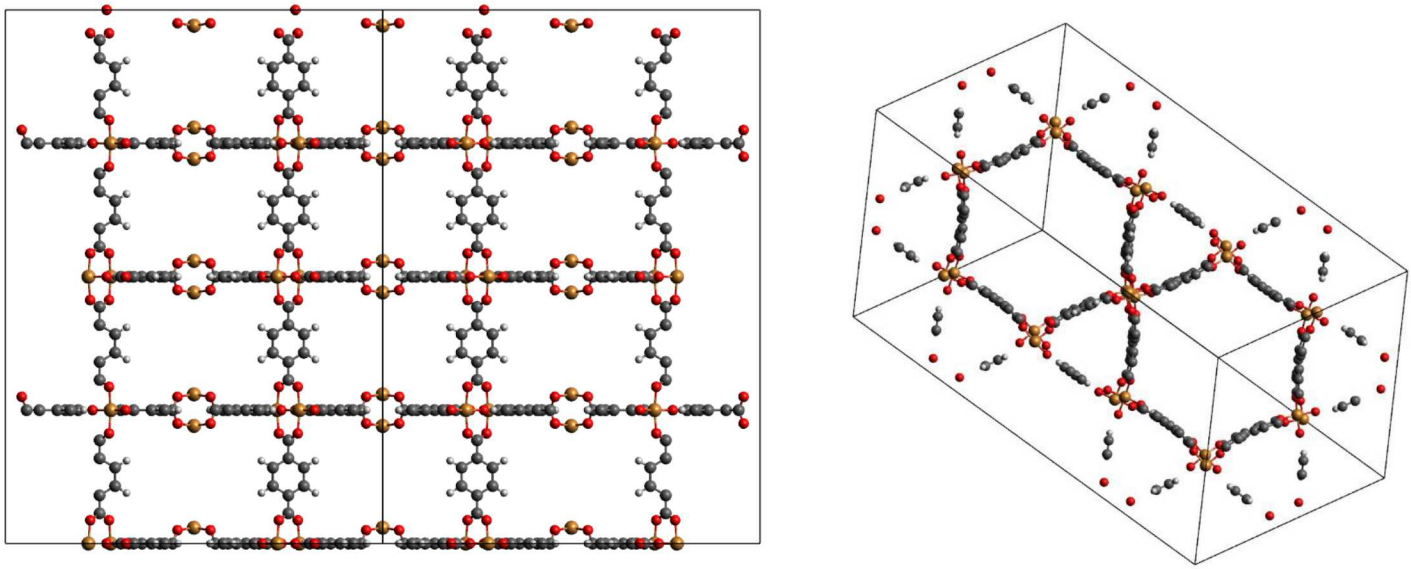

a b

Figure 8: Visualization of the a) cubic, along [100] axis, and b) star conformations of nbo_L12, looking down 1D channels which are almost aligned with the [001] axis. Grey spheres are H, red spheres are O, orange spheres are Cu, and small white spheres are H.

The origins of the 1D hexagonal channels in the star conformation of nbo_L12 can be seen by looking down the [111] direction of the cubic conformation as seen in Figure 9. The star conformation is formed by compressing the MOF along the [111] vector and twisting the nodes and linkers to open up the triangular channels. An animated movie of this transformation is available in the Supplemental Information. The cubic conformation contains alternating Cu-paddlewheel nodes, and each node is orthogonal to its neighbors (defined by the vector lying along the Cu−Cu direction). This is clearly seen in Figure 8a. In the star confirmation, each Cu-paddlewheel node lies at a 35-degree angle to its neighbor.

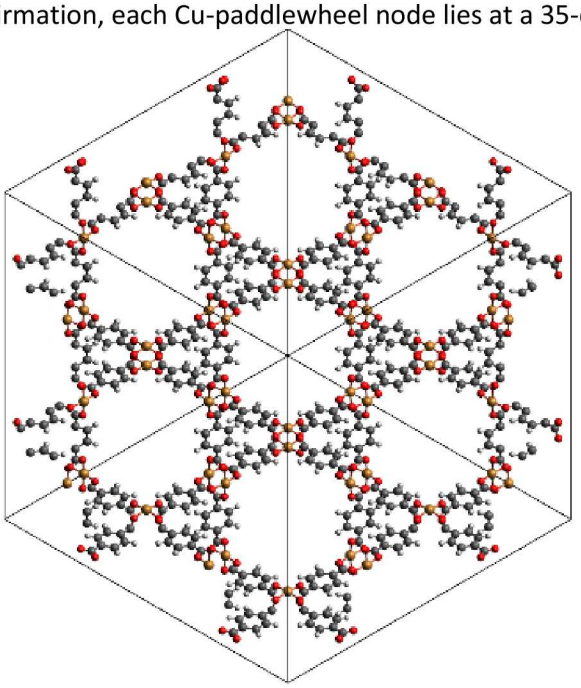

Figure 9: Visualization of nbo_L12 in the cubic conformation, viewed down the [111] direction. Gray atoms are C, orange are Cu, red are O, and white are H.

The star conformation can be obtained from the cubic conformation via a simple structural minimization. Figure 10 shows snapshots of a minimization calculation (using the force field) starting with the cubic conformation and ending with the star conformation. No bonds are broken during this calculation. As the calculation progresses, one can see how the shape of the cubic unit cell becomes skewed and the 1D channels begin to form, nearly (albeit not perfectly) aligned with the z-axis. Structural files for both conformations of nbo_L12 and intermediate steps of the geometric optimization are available in the Supplemental Information.

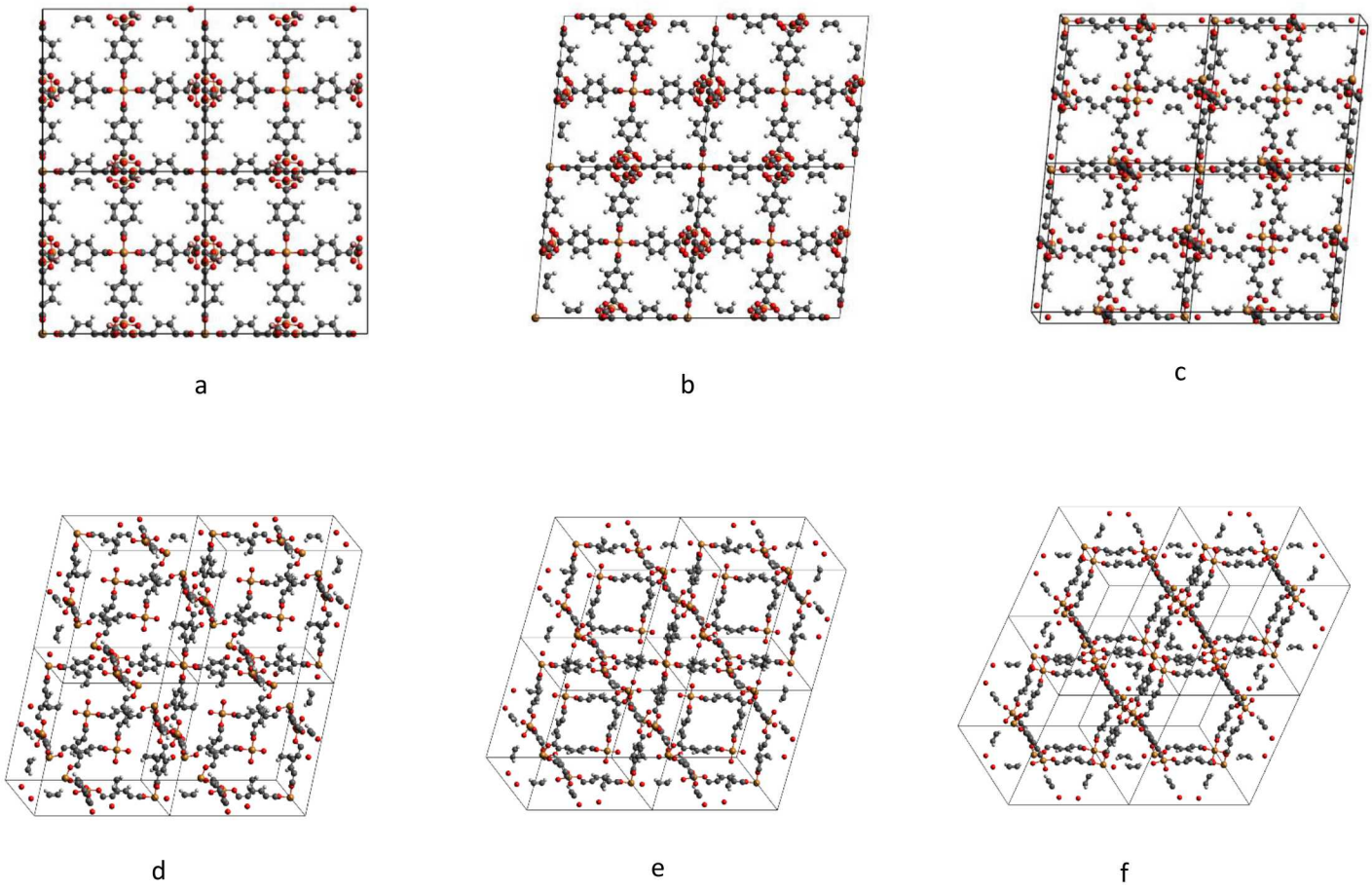

Figure 10: Visualized snapshots looking along the [001] axis from a geometric optimization of nbo_L12 using the universal force field. The structure starts off in the a) cubic conformation and passes through the intermediate structures shown in b, c, d, and e, ending with f) the star conformation. An animated movie of this optimization is available in the Supplemental Information.

We used DFT calculations to compare the energetic favorability of the two nbo_L12 conformations. Since the structures are chemically identical, a simple comparison of the potential energy of each structure in its local minimum gives a reasonable idea of which one is more favorable. We report the energy normalized by the formula unit of the crystal, $CuC_8H_4O_4$. The DFT calculations indicate that the star conformation of nbo_L12 is 31.5 kJ/mol per formula unit more favorable than the cubic conformation. For this calculation we used a cell containing 12 formula units per cell for the star conformation and 6 formula units for the cubic conformation, which are the smallest possible cells based on the symmetry of the crystals.

Not all other **nbo** MOFs from the same database[28] with similar composition favor the star conformation. For example, adding a single alkyne spacer to the BDC (BDC = benzene-1,4-dicarboxylic acid) edge of nbo_L12 creates a new MOF, nbo_L20 (Figure 11b). nbo_L20 remains in the cubic conformation upon minimization. However, changing the BDC edge to a pyrene (nbo_L22) again results in the star conformation (Figure 11c). DFT calculations indicate that the star conformation of nbo_L22 is 13.9 kJ/mol per formula unit ($CuC_{18}H_8O_4$) more favorable than the cubic conformation. As before, we used 12 formula units in the cell for the star conformation and 6 formula units for the cubic conformation.

The factor that determines if the **nbo** MOF prefers the cubic conformation or the star conformation is the steric hindrance between the Cu-paddlewheel node and the linker. A single phenyl ring on a single Cu-paddlewheel node prefers to lie in the plane of the carboxylic acids. However, in the cubic conformation **nbo** topology, alternating nodes are orthogonal to each other (Figure 8a); therefore, the linker cannot be aligned with them both. This puts strain on the framework and twists it into the star conformation, where the steric hindrance between the edge and nodes is reduced. The same is true for the pyrene edge L_22 because it is a rigid edge that couples the neighboring Cu nodes via steric hindrance. If an alkyne spacer is added (L20) the Cu node is sufficiently far away from the phenyl ring that it is not coupled to its neighbor (Figure 11d). This structure tends to remain in the cubic conformation.

Interestingly, an edge with two independent phenyl rings (L24) results in a weaker coupling of the Cu nodes. This structure is slightly skewed from the cubic conformation but also not completely transformed into the star conformation. This demonstrates how the choice of linkers can greatly affect the structure of the crystal through steric interactions with the node. This behavior could afford a good opportunity for future research into the effects of flexibility in these MOFs. It would be interesting to study how the steric effects of different linker influence the flexibility of the MOF and how that relationship is affected by the presence of adsorbates. However, our focus in this work is on topological effects on separations, so we did not pursue flexibility further.

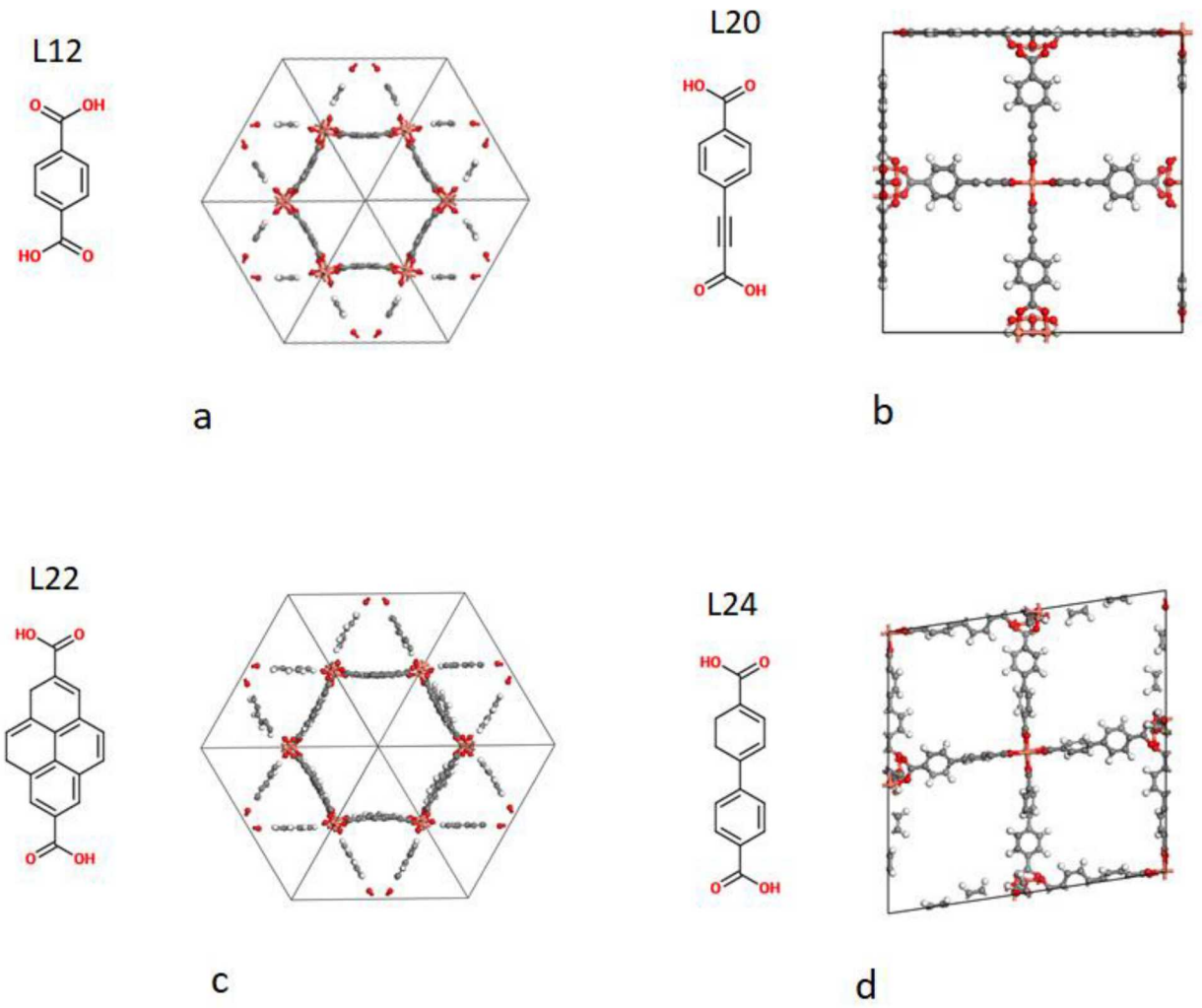

Figure 11: Visualization of four edges and the resulting **nbo** *MOF. a) L12 and c) L22 form the star conformation due to steric coupling of the Cu nodes. b) L20 remains in the cubic conformation. d) L24 results in weak coupling of the nodes and only partially skews the MOF away from the true cubic conformation.*

3.6 Thermodynamic Comparison of Polymorphs

Given that MOF polymorphs are made from the same chemical building blocks, it is a challenging task to control the synthesis process to obtain the desired topology. Since the nbo_L12 MOF in particular shows promise for separation applications, here we consider the plausibility of synthesizing this topology instead of the **lvt** or **rhr** variants.

Since polymorphic MOFs are framework isomers and have the same chemical formula, we can compare the energies of minimized structures directly. We performed structural optimizations using DFT in VASP for nbo_L12 and lvt_L12. However, the unit cell of rhr_L12 is too large for DFT calculations, so we also did structural optimizations for all three (nbo_L12, lvt_L12, and rhr_L12) using UFF in Materials Studio. The results are shown in Table 7.

DFT calculations indicate that, based on the formula unit $CuC_8H_4O_4$, nbo_L12 is 0.13 eV (12.2 kJ/mol) per formula unit more favorable than lvt_L12. Using UFF, lvt_L12 is the most favorable, although it is only 0.01 eV (1.2 kJ/mol) per formula unit different than nbo_L12. Based on UFF calculations, rhr_L12 is the least favorable being 0.18 eV (17.7 kJ/mol) per formula unit less favored than the **lvt** MOF. While this analysis is only a first approximation, it gives us reason to believe that synthesizing nbo_L12 may be feasible.

Table 7: Energy differences (in kJ/mol) per formula unit of three MOFs, relative to nbo_L12. The formula unit for all three MOFs is $CuC_8H_4O_4$.

MOF	UFF	DFT
nbo_L12	0	0
lvt_L12	-1.2	12.2
rhr_l12	17.7	-

4. Conclusion

We have demonstrated that the topology of a MOF can greatly influence its adsorption behavior via changes to the pore structure, which has implications for chemical separations. We have shown that within the **nbo/rhr/lvt** polymorph family, the choice of topology can change or even invert the selectivity for the separation of alkane isomers. The MOF Cu_2(1,4-benzenedicarboxylate) in **nbo** topology (nbo-Cu_2BDC) shows especially high affinity for normal isomers, *n*-pentane and *n*-hexane, due to size exclusion within its small triangular channels that are inaccessible to bulkier branched isomers. rhr-Cu_2BDC is moderately selective for the branched isomers due to higher enthalpic favorability. We also find that nbo-Cu_2BDC can adopt a unique star conformation, which results in triangular and hexagonal 1D channels in a Kagome lattice. This conformation depends on steric effects between the linker and the paddlewheel nodes. Rigid linkers, such as phenyl or pyrene, couple the neighboring nodes and strain the lattice so that it forms the star conformation, while linkers with alkynes adjacent to the nodes form the cubic conformation. This demonstrates that even for MOFs with the same topology, there can be significantly different pore shapes and structures, which influences adsorption behavior for separations.

5. Acknowledgements

This work was supported by the Defense Threat Reduction Agency (Grant HDTRA1-19-1-0007). A.S.R. was supported in part by a fellowship award through the National Defense Science and Engineering Graduate (NDSEG) Fellowship Program, sponsored by the Air Force Research Laboratory (AFRL), the Office of Naval Research (ONR) and the Army Research Office (ARO). A.S.R. also gratefully acknowledges support from a Ryan Fellowship and the International Institute for Nanotechnology at Northwestern University. This research was supported in part through the computational resources and staff contributions provided for the Quest high performance computing facility at Northwestern University

which is jointly supported by the Office of the Provost, the Office for Research, and Northwestern University Information Technology. Sandia National Laboratories is a multimission laboratory managed and operated by National Technology and Engineering Solutions of Sandia, LLC., a wholly owned subsidiary of Honeywell International, Inc., for the U.S. Department of Energy's National Nuclear Security Administration under contract DE-NA0003525. This paper describes objective technical results and analysis. Any subjective views or opinions that might be expressed in the paper do not necessarily represent the views of the U.S. Department of Energy or the United States Government.

6. References

1. Wilmer, C. E.; Leaf, M.; Lee, C. Y.; Farha, O. K.; Hauser, B. G.; Hupp, J. T.; Snurr, R. Q., Large-Scale Screening of Hypothetical Metal–Organic Frameworks. *Nature Chemistry* **2012**, *4*, 83.
2. Bobbitt, N. S.; Chen, J.; Snurr, R. Q., High-Throughput Screening of Metal–Organic Frameworks for Hydrogen Storage at Cryogenic Temperature. *The Journal of Physical Chemistry C* **2016**, *120*, 27328-27341.
3. Fernandez, M.; Boyd, P. G.; Daff, T. D.; Aghaji, M. Z.; Woo, T. K., Rapid and Accurate Machine Learning Recognition of High Performing Metal Organic Frameworks for Co_2 Capture. *The Journal of Physical Chemistry Letters* **2014**, *5*, 3056-3060.
4. Eddaoudi, M.; Kim, J.; Rosi, N.; Vodak, D.; Wachter, J.; O'Keeffe, M.; Yaghi, O. M., Systematic Design of Pore Size and Functionality in Isoreticular Mofs and Their Application in Methane Storage. *Science* **2002**, *295*, 469-472.
5. Islamoglu, T.; Otake, K.-i.; Li, P.; Buru, C. T.; Peters, A. W.; Akpinar, I.; Garibay, S. J.; Farha, O. K., Revisiting the Structural Homogeneity of Nu-1000, a Zr-Based Metal–Organic Framework. *CrystEngComm* **2018**, *20*, 5913-5918.
6. Torrisi, A.; Bell, R. G.; Mellot-Draznieks, C., Functionalized Mofs for Enhanced Co_2 Capture. *Crystal growth & design* **2010**, *10*, 2839-2841.
7. Aulakh, D.; Varghese, J. R.; Wriedt, M., The Importance of Polymorphism in Metal–Organic Framework Studies. *Inorganic Chemistry* **2015**, *54*, 8679-8684.
8. Bon, V.; Senkovska, I.; Baburin, I. A.; Kaskel, S., Zr-and Hf-Based Metal–Organic Frameworks: Tracking Down the Polymorphism. *Crystal Growth & Design* **2013**, *13*, 1231-1237.
9. Zhu, N.; Lennox, M. J.; Düren, T.; Schmitt, W., Polymorphism of Metal–Organic Frameworks: Direct Comparison of Structures and Theoretical N_2 Uptake of Topological Pto-and Tbo-Isomers. *Chemical Communications* **2014**, *50*, 4207-4210.
10. Tanasaro, T.; Adpakpang, K.; Ittisanronnachai, S.; Faungnawakij, K.; Butburee, T.; Wannapaiboon, S.; Ogawa, M.; Bureekaew, S., Control of Polymorphism of Metal–Organic Frameworks Using Mixed-Metal Approach. *Crystal Growth & Design* **2017**, *18*, 16-21.
11. Frahm, D.; Hoffmann, F.; Fröba, M., Two Metal–Organic Frameworks with a Tetratopic Linker: Solvent-Dependent Polymorphism and Postsynthetic Bromination. *Crystal Growth & Design* **2014**, *14*, 1719-1725.
12. Karadeniz, B.; Žilić, D.; Huskić, I.; Germann, L. S.; Muratović, S.; Lončarić, I.; Etter, M.; Dinnebier, R.; Barišić, D.; Cindro, N., Controlling the Polymorphism and Topology Transformation in Porphyrinic Zirconium Metal-Organic Frameworks Via Mechanochemistry. *Journal of the American Shemical Society* **2019**, *141*, 19214-19220.
13. Kieslich, G.; Kumagai, S.; Butler, K. T.; Okamura, T.; Hendon, C. H.; Sun, S.; Yamashita, M.; Walsh, A.; Cheetham, A. K., Role of Entropic Effects in Controlling the Polymorphism in Formate Abx 3 Metal–Organic Frameworks. *Chemical Communications* **2015**, *51*, 15538-15541.
14. Herm, Z. R.; Bloch, E. D.; Long, J. R., Hydrocarbon Separations in Metal–Organic Frameworks. *Chemistry of Materials* **2014**, *26*, 323-338.
15. Leffler, W. L., *Petroleum Refining in Nontechnical Language*; PennWell Books, 2008.
16. Curran, H. J.; Gaffuri, P.; Pitz, W. J.; Westbrook, C. K.; Leppard, W. R., Autoignition Chemistry of the Hexane Isomers: An Experimental and Kinetic Modeling Study. *SAE transactions* **1995**, 1184-1195.
17. Piehl, J.; Zyada, A.; Bravo, L.; Samimi-Abianeh, O., Review of Oxidation of Gasoline Surrogates and Its Components. *Journal of Combustion* **2018**, *2018*.
18. Ono, Y., A Survey of the Mechanism in Catalytic Isomerization of Alkanes. *Catalysis Today* **2003**, *81*, 3-16.

19. Jiang, J.; Sandler, S. I., Monte Carlo Simulation for the Adsorption and Separation of Linear and Branched Alkanes in Irmof-1. *Langmuir* **2006**, *22*, 5702-5707.
20. Chung, Y. G.; Bai, P.; Haranczyk, M.; Leperi, K. T.; Li, P.; Zhang, H.; Wang, T. C.; Duerinck, T.; You, F.; Hupp, J. T., Computational Screening of Nanoporous Materials for Hexane and Heptane Isomer Separation. *Chemistry of Materials* **2017**, *29*, 6315-6328.
21. Herm, Z. R.; Wiers, B. M.; Mason, J. A.; van Baten, J. M.; Hudson, M. R.; Zajdel, P.; Brown, C. M.; Masciocchi, N.; Krishna, R.; Long, J. R., Separation of Hexane Isomers in a Metal-Organic Framework with Triangular Channels. *Science* **2013**, *340*, 960-964.
22. Mukherjee, S.; Desai, A. V.; Ghosh, S. K., Potential of Metal–Organic Frameworks for Adsorptive Separation of Industrially and Environmentally Relevant Liquid Mixtures. *Coordination Chemistry Reviews* **2018**, *367*, 82-126.
23. Dubbeldam, D.; Krishna, R.; Calero, S.; Yazaydın, A. Ö., Computer-Assisted Screening of Ordered Crystalline Nanoporous Adsorbents for Separation of Alkane Isomers. *Angewandte Chemie International Edition* **2012**, *51*, 11867-11871.
24. Duerinck, T.; Bueno-Perez, R.; Vermoortele, F.; De Vos, D.; Calero, S.; Baron, G.; Denayer, J., Understanding Hydrocarbon Adsorption in the Uio-66 Metal–Organic Framework: Separation of (Un) Saturated Linear, Branched, Cyclic Adsorbates, Including Stereoisomers. *The Journal of Physical Chemistry C* **2013**, *117*, 12567-12578.
25. Jiang, J.; Sandler, S. I.; Schenk, M.; Smit, B., Surface Physics, Nanoscale Physics, Low-Dimensional Systems-Adsorption and Separation of Linear and Branched Alkanes on Carbon Nanotube Bundles from Configurational-Bias Monte Carlo Simulation. *Physical Review-Section B-Condensed Matter* **2005**, *72*, 45447-45447.
26. Herrera-Herrera, A. V.; González-Curbelo, M. Á.; Hernández-Borges, J.; Rodríguez-Delgado, M. Á., Carbon Nanotubes Applications in Separation Science: A Review. *Analytica Chimica Acta* **2012**, *734*, 1-30.
27. Krishna, R.; Smit, B.; Calero, S., Entropy Effects During Sorption of Alkanes in Zeolites. *Chemical Society Reviews* **2002**, *31*, 185-194.
28. Colón, Y. J.; Gómez-Gualdrón, D. A.; Snurr, R. Q., Topologically Guided, Automated Construction of Metal–Organic Frameworks and Their Evaluation for Energy-Related Applications. *Crystal Growth & Design* **2017**, *17*, 5801-5810.
29. Accelrys, I., Materials Studio. *Accelrys Software Inc* **2010**.
30. Rappé, A. K.; Casewit, C. J.; Colwell, K.; Goddard III, W. A.; Skiff, W. M., Uff, a Full Periodic Table Force Field for Molecular Mechanics and Molecular Dynamics Simulations. *Journal of the American Chemical Society* **1992**, *114*, 10024-10035.
31. Bucior, B. J.; Rosen, A. S.; Haranczyk, M.; Yao, Z.; Ziebel, M. E.; Farha, O. K.; Hupp, J. T.; Siepmann, J. I.; Aspuru-Guzik, A.; Snurr, R. Q., Identification Schemes for Metal–Organic Frameworks to Enable Rapid Search and Cheminformatics Analysis. *Crystal Growth & Design* **2019**, *19*, 6682-6697.
32. Dubbeldam, D.; Calero, S.; Ellis, D. E.; Snurr, R. Q., Raspa: Molecular Simulation Software for Adsorption and Diffusion in Flexible Nanoporous Materials. *Molecular Simulation* **2016**, *42*, 81-101.
33. Martin, M. G.; Siepmann, J. I., Transferable Potentials for Phase Equilibria. 1. United-Atom Description of N-Alkanes. *The Journal of Physical Chemistry B* **1998**, *102*, 2569-2577.
34. Willems, T. F.; Rycroft, C. H.; Kazi, M.; Meza, J. C.; Haranczyk, M., Algorithms and Tools for High-Throughput Geometry-Based Analysis of Crystalline Porous Materials. *Microporous and Mesoporous Materials* **2012**, *149*, 134-141.
35. Pinheiro, M.; Martin, R. L.; Rycroft, C. H.; Jones, A.; Iglesia, E.; Haranczyk, M., Characterization and Comparison of Pore Landscapes in Crystalline Porous Materials. *Journal of Molecular Graphics and Modelling* **2013**, *44*, 208-219.

36. Linstrom, P. J.; Mallard, W. G., The Nist Chemistry Webbook: A Chemical Data Resource on the Internet. *Journal of Chemical & Engineering Data* **2001**, *46*, 1059-1063.
37. Kresse, G.; Furthmüller, J., Efficient Iterative Schemes for Ab Initio Total-Energy Calculations Using a Plane-Wave Basis Set. *Physical Review B* **1996**, *54*, 11169.
38. Kresse, G.; Joubert, D., From Ultrasoft Pseudopotentials to the Projector Augmented-Wave Method. *Physical Review B* **1999**, *59*, 1758.
39. Perdew, J. P.; Burke, K.; Ernzerhof, M., Generalized Gradient Approximation Made Simple. *Physical review letters* **1996**, *77*, 3865.
40. Grimme, S.; Antony, J.; Ehrlich, S.; Krieg, H., A Consistent and Accurate Ab Initio Parametrization of Density Functional Dispersion Correction (Dft-D) for the 94 Elements H-Pu. *The Journal of Chemical Physics* **2010**, *132*, 154104.
41. Grimme, S.; Ehrlich, S.; Goerigk, L., Effect of the Damping Function in Dispersion Corrected Density Functional Theory. *Journal of Computational Chemistry* **2011**, *32*, 1456-1465.
42. Blöchl, P. E., Projector Augmented-Wave Method. *Physical Review B* **1994**, *50*, 17953.
43. Nazarian, D.; Ganesh, P.; Sholl, D. S., Benchmarking Density Functional Theory Predictions of Framework Structures and Properties in a Chemically Diverse Test Set of Metal–Organic Frameworks. *Journal of Materials Chemistry A* **2015**, *3*, 22432-22440.
44. Formalik, F.; Fischer, M.; Rogacka, J.; Firlej, L.; Kuchta, B., Benchmarking of Gga Density Functionals for Modeling Structures of Nanoporous, Rigid and Flexible Mofs. *The Journal of Chemical Physics* **2018**, *149*, 064110.
45. Rosen, A. S.; Notestein, J. M.; Snurr, R. Q., Identifying Promising Metal–Organic Frameworks for Heterogeneous Catalysis Via High-Throughput Periodic Density Functional Theory. *Journal of Computational Chemistry* **2019**, *40*, 1305-1318.
46. Ong, S. P.; Richards, W. D.; Jain, A.; Hautier, G.; Kocher, M.; Cholia, S.; Gunter, D.; Chevrier, V. L.; Persson, K. A.; Ceder, G., Python Materials Genomics (Pymatgen): A Robust, Open-Source Python Library for Materials Analysis. *Computational Materials Science* **2013**, *68*, 314-319.
47. Teter, M. P.; Payne, M. C.; Allan, D. C., Solution of Schrödinger's Equation for Large Systems. *Physical Review B* **1989**, *40*, 12255.
48. Bylander, D.; Kleinman, L.; Lee, S., Self-Consistent Calculations of the Energy Bands and Bonding Properties of B 12 C 3. *Physical Review B* **1990**, *42*, 1394.
49. Bylander, D.; Kleinman, L.; Lee, S., Erratum: Self-Consistent Calculations of the Energy Bands and Bonding Properties of B 12 C 3. *Physical Review B* **1993**, *47*, 10056.
50. Freysoldt, C.; Boeck, S.; Neugebauer, J., Direct Minimization Technique for Metals in Density Functional Theory. *Physical Review B* **2009**, *79*, 241103.
51. Hendon, C. H.; Walsh, A., Chemical Principles Underpinning the Performance of the Metal–Organic Framework Hkust-1. *Chemical Science* **2015**, *6*, 3674-3683.
52. Tiana, D.; Hendon, C. H.; Walsh, A., Ligand Design for Long-Range Magnetic Order in Metal–Organic Frameworks. *Chemical Communications* **2014**, *50*, 13990-13993.
53. Shen, L.; Yang, S.-W.; Xiang, S.; Liu, T.; Zhao, B.; Ng, M.-F.; Göettlicher, J. r.; Yi, J.; Li, S.; Wang, L., Origin of Long-Range Ferromagnetic Ordering in Metal–Organic Frameworks with Antiferromagnetic Dimeric-Cu (Ii) Building Units. *Journal of the American Chemical Society* **2012**, *134*, 17286-17290.
54. Tafipolsky, M.; Amirjalayer, S.; Schmid, R., First-Principles-Derived Force Field for Copper Paddle-Wheel-Based Metal− Organic Frameworks. *The Journal of Physical Chemistry C* **2010**, *114*, 14402-14409.
55. Peralta, D.; Chaplais, G. r.; Simon-Masseron, A. l.; Barthelet, K.; Pirngruber, G. D., Separation of C6 Paraffins Using Zeolitic Imidazolate Frameworks: Comparison with Zeolite 5a. *Industrial & Engineering Chemistry Research* **2012**, *51*, 4692-4702.
56. Kulprathipanja, S., *Zeolites in Industrial Separation and Catalysis*; John Wiley & Sons, 2010.

57. Chen, B.; Ockwig, N. W.; Millward, A. R.; Contreras, D. S.; Yaghi, O. M., High H2 Adsorption in a Microporous Metal–Organic Framework with Open Metal Sites. *Angewandte Chemie International Edition* **2005**, *44*, 4745-4749.
58. Seo, J.; Jin, N.; Chun, H., Topologies of Metal− Organic Frameworks Based on Pyrimidine-5-Carboxylate and Unexpected Gas-Sorption Selectivity for Co2. *Inorganic Chemistry* **2010**, *49*, 10833-10839.
59. Zhang, Z.; Wojtas, L.; Zaworotko, M. J., Consequences of Partial Flexibility in 1, 3-Benzenedicarboxylate Linkers: Kagome Lattice and Nbo Supramolecular Isomers from Complexation of a Bulky 1, 3-Benzenedicarboxylate to Cu (Ii) Paddlewheel Moieties. *Crystal Growth & Design* **2011**, *11*, 1441-1445.

Topological Effects on Separation of Alkane Isomers in Metal-Organic Frameworks

Supplemental Information

N. Scott Bobbitt[1], Andrew S. Rosen[2], and Randall Q. Snurr*[2]

1. Sandia National Laboratories, Albuquerque, New Mexico, 87185

2. Department of Chemical and Biological Engineering, Northwestern University, Evanston, Illinois, 60208

**Corresponding author: snurr@northwestern.edu*

Topological Diagrams

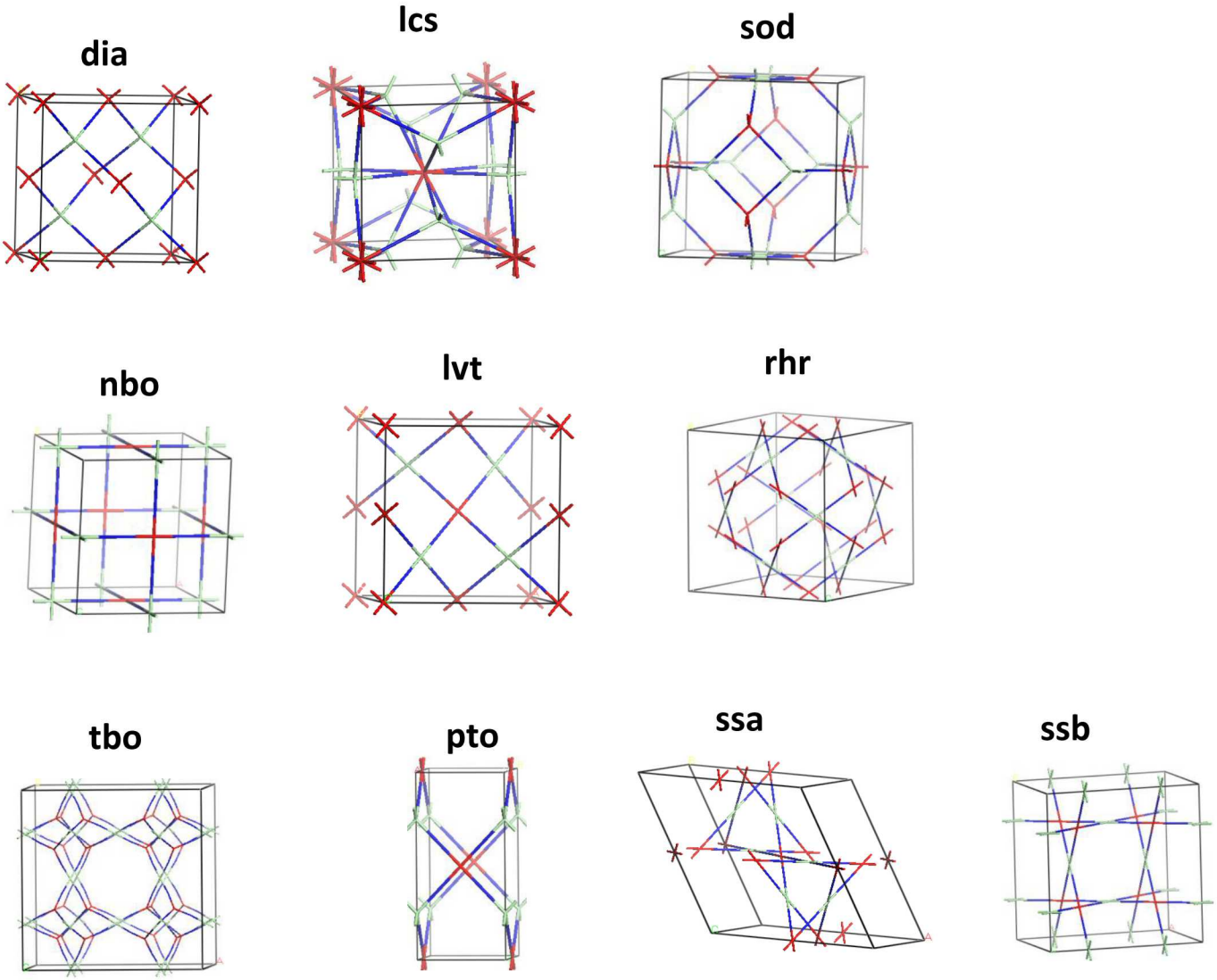

Supplemental Figure 1: Diagrams of the topological nets used for the MOFs in this work. Adapted with permission from Colón and Gómez-Gualdrón et al. Cryst. Growth Des. 2017, **17***, 11, 5801-5810. Copyright 2017 American Chemical Society.*

MOFids and MOFkeys

Supplemental Table 1: MOFids and MOFkeys for the 39 MOFs discussed in this work. These unique strings that describe each MOF are based on the work of Bucior et al., Cryst. Growth Des. 2019, 19, 11, 6682-6697.

MOF Name	MOFid	MOFkey
diab_sym_4_mc_1_sym_4_mc_1_L_12	[Zn].n1ccc(cc1)c1ccc(cc1)c1ccncc1 MOFid-v1.dia.cat0;diab_sym_4_mc_1_sym_4_mc_1_L_12	Zn.MAWKLXRVKVOYLR.MOFkey-v1.dia
diab_sym_4_mc_1_sym_4_mc_1_L_20	[Zn].n1ccc(cc1)C#Cc1ccc(cc1)c1ccncc1 MOFid-v1.dia.cat0;diab_sym_4_mc_1_sym_4_mc_1_L_20	Zn.FUHZYCVAWBTDTQ.MOFkey-v1.dia
diab_sym_4_mc_1_sym_4_mc_1_L_24	[Zn].n1ccc(cc1)c1ccc(cc1)c1ccc(cc1)c1ccncc1 MOFid-v1.dia.cat0;diab_sym_4_mc_1_sym_4_mc_1_L_24	Zn.RERPRBPQDPHWCZ.MOFkey-v1.dia
diab_sym_4_mc_1_sym_4_mc_1_L_3	[Zn].n1ccc(cc1)C#Cc1ccncc1 MOFid-v1.dia.cat0;diab_sym_4_mc_1_sym_4_mc_1_L_3	Zn.SPKCEACOZLCRSV.MOFkey-v1.dia
lcsb_sym_4_mc_1_sym_4_mc_1_L_12	[Zn].n1ccc(cc1)c1ccc(cc1)c1ccncc1 MOFid-v1.lcs.cat0;lcsb_sym_4_mc_1_sym_4_mc_1_L_12	Zn.MAWKLXRVKVOYLR.MOFkey-v1.lcs
lcsb_sym_4_mc_1_sym_4_mc_1_L_20	[Zn].n1ccc(cc1)C#Cc1ccc(cc1)c1ccncc1 MOFid-v1.lcs.cat0;lcsb_sym_4_mc_1_sym_4_mc_1_L_20	Zn.FUHZYCVAWBTDTQ.MOFkey-v1.lcs
lcsb_sym_4_mc_1_sym_4_mc_1_L_24	[Zn].n1ccc(cc1)c1ccc(cc1)c1ccc(cc1)c1ccncc1 MOFid-v1.lcs.cat0;lcsb_sym_4_mc_1_sym_4_mc_1_L_24	Zn.RERPRBPQDPHWCZ.MOFkey-v1.lcs
lcsb_sym_4_mc_1_sym_4_mc_1_L_3	[Zn].n1ccc(cc1)C#Cc1ccncc1 MOFid-v1.lcs.cat0;lcsb_sym_4_mc_1_sym_4_mc_1_L_3	Zn.SPKCEACOZLCRSV.MOFkey-v1.lcs
lvtb_sym_5_mc_2_sym_5_mc_2_L_12	[Cu][Cu].[O-]C(=O)c1ccc(cc1)C(=O)[O-] MOFid-v1.lvt.cat0;lvtb_sym_5_mc_2_sym_5_mc_2_L_12	Cu.KKEYFWRCBNTPAC.MOFkey-v1.lvt
lvtb_sym_5_mc_2_sym_5_mc_2_L_20	[Cu][Cu].[O-]C(=O)C#Cc1ccc(cc1)C(=O)[O-] MOFid-v1.lvt.cat0;lvtb_sym_5_mc_2_sym_5_mc_2_L_20	Cu.ZDVLJCAJPABTSV.MOFkey-v1.lvt
lvtb_sym_5_mc_2_sym_5_mc_2_L_24	[Cu][Cu].[O-]C(=O)c1ccc(cc1)c1ccc(cc1)C(=O)[O-] MOFid-v1.lvt.cat0;lvtb_sym_5_mc_2_sym_5_mc_2_L_24	Cu.NEQFBGHQPUXOFH.MOFkey-v1.lvt
lvtb_sym_5_mc_2_sym_5_mc_2_L_3	[Cu][Cu].[O-]C(=O)C#CC(=O)[O-] MOFid-v1.lvt.cat0;lvtb_sym_5_mc_2_sym_5_mc_2_L_3	Cu.YTIVTFGABIZHHX.MOFkey-v1.lvt
nbob_sym_5_mc_2_sym_5_mc_2_L_12	[Cu][Cu].[O-]C(=O)c1ccc(cc1)C(=O)[O-] MOFid-v1.nbo.cat0;nbob_sym_5_mc_2_sym_5_mc_2_L_12	Cu.KKEYFWRCBNTPAC.MOFkey-v1.nbo
nbob_sym_5_mc_2_sym_5_mc_2_L_20	[Cu][Cu].[O-]C(=O)C#Cc1ccc(cc1)C(=O)[O-] MOFid-v1.nbo.cat0;nbob_sym_5_mc_2_sym_5_mc_2_L_20	Cu.ZDVLJCAJPABTSV.MOFkey-v1.nbo
nbob_sym_5_mc_2_sym_5_mc_2_L_22	[Cu][Cu].[O-]C(=O)c1cc2ccc3c4c2c(c1)ccc4cc(c3)C(=O)[O-] MOFid-v1.nbo.cat0;nbob_sym_5_mc_2_sym_5_mc_2_L_22	Cu.OTAJGWQCQIEFEV.MOFkey-v1.nbo
nbob_sym_5_mc_2_sym_5_mc_2_L_24	[Cu][Cu].[O-]C(=O)c1ccc(cc1)c1ccc(cc1)C(=O)[O-] MOFid-v1.nbo.cat0;nbob_sym_5_mc_2_sym_5_mc_2_L_24	Cu.NEQFBGHQPUXOFH.MOFkey-v1.nbo
nbob_sym_5_mc_2_sym_5_mc_2_L_3	[Cu][Cu].[O-]C(=O)C#CC(=O)[O-] MOFid-v1.nbo.cat0;nbob_sym_5_mc_2_sym_5_mc_2_L_3	Cu.YTIVTFGABIZHHX.MOFkey-v1.nbo
pto_sym_3_on_2_sym_5_mc_2_L_12	[Cu][Cu].[O-]C(=O)c1ccc(cc1)c1cc(cc(c1)c1ccc(cc1)C(=O)[O-])c1ccc(cc1)C(=O)[O-] MOFid-v1.pto,dia.cat0;pto_sym_3_on_2_sym_5_mc_2_L_12	Cu.SATWKVZGMWCXOJ.MOFkey-v1.pto
pto_sym_3_on_2_sym_5_mc_2_L_20	[Cu][Cu].[O-]C(=O)c1ccc(cc1)C#Cc1cc(C#Cc2ccc(cc2)C(=O)[O-])cc(c1)C#Cc1ccc(cc1)C(=O)[O-] MOFid-v1.pto,dia.cat0;pto_sym_3_on_2_sym_5_mc_2_L_20	Cu.NIJMZBWVSRWZFZ.MOFkey-v1.pto
pto_sym_3_on_2_sym_5_mc_2_L_24	[Cu][Cu].[O-]C(=O)c1ccc(cc1)c1ccc(cc1)c1cc(cc(c1)c1ccc(cc1)c1ccc(cc1)C(=O)[O-])c1ccc(cc1)c1ccc(cc1)C(=O)[O-] MOFid-v1.dia.cat0;pto_sym_3_on_2_sym_5_mc_2_L_24	Zn.RERPRBPQDPHWCZ.MOFkey-v1.dia
pto_sym_3_on_2_sym_5_mc_2_L_3	[Cu][Cu].[O-]C(=O)C#Cc1cc(C#CC(=O)[O-])cc(c1)C#CC(=O)[O-] MOFid-v1.pto.cat0;pto_sym_3_on_2_sym_5_mc_2_L_3	Cu.KHRUPMNUDNAAJH.MOFkey-v1.pto
rhrb_sym_5_mc_2_sym_5_mc_2_L_12	[Cu][Cu].[O-]C(=O)c1ccc(cc1)C(=O)[O-] MOFid-v1.rhr.cat0;rhrb_sym_5_mc_2_sym_5_mc_2_L_12	Cu.KKEYFWRCBNTPAC.MOFkey-v1.rhr

rhrb_sym_5_mc_2_sym_5_mc_2_L_20	[Cu][Cu].[O-]C(=O)C#Cc1ccc(cc1)C(=O)[O-] MOFid-v1.lcs.cat0;rhrb_sym_5_mc_2_sym_5_mc_2_L_20	Cu.ZDVLJCAJPABTSV.MOFkey-v1.lcs
rhrb_sym_5_mc_2_sym_5_mc_2_L_24	[Cu][Cu].[O-]C(=O)c1ccc(cc1)c1ccc(cc1)C(=O)[O-] MOFid-v1.lcs.cat0;rhrb_sym_5_mc_2_sym_5_mc_2_L_24	Cu.NEQFBGHQPUXOFH.MOFkey-v1.lcs
rhrb_sym_5_mc_2_sym_5_mc_2_L_3	[Cu][Cu].[O-]C(=O)C#CC(=O)[O-] MOFid-v1.lcs.cat0;rhrb_sym_5_mc_2_sym_5_mc_2_L_3	Zn.SPKCEACOZLCRSV.MOFkey-v1.lcs
sodb_sym_4_mc_1_sym_4_mc_1_L_12	[Zn].n1ccc(cc1)c1ccc(cc1)c1ccncc1 MOFid-v1.sod.cat0;sodb_sym_4_mc_1_sym_4_mc_1_L_12	Zn.MAWKLXRVKVOYLR.MOFkey-v1.sod
sodb_sym_4_mc_1_sym_4_mc_1_L_20	[Zn].n1ccc(cc1)C#Cc1ccc(cc1)c1ccncc1 MOFid-v1.sod,lvt.cat0;sodb_sym_4_mc_1_sym_4_mc_1_L_20	Zn.FUHZYCVAWBTDTQ.MOFkey-v1.sod
sodb_sym_4_mc_1_sym_4_mc_1_L_24	[Zn].n1ccc(cc1)c1ccc(cc1)c1ccc(cc1)c1ccncc1 MOFid-v1.sod.cat0;sodb_sym_4_mc_1_sym_4_mc_1_L_24	Cu.YTIVTFGABIZHHX.MOFkey-v1.sod
sodb_sym_4_mc_1_sym_4_mc_1_L_3	[Zn].n1ccc(cc1)C#Cc1ccncc1 MOFid-v1.sod.cat0;sodb_sym_4_mc_1_sym_4_mc_1_L_3	Zn.SPKCEACOZLCRSV.MOFkey-v1.sod
ssa_sym_5_mc_2_sym_5_on_9_L_15	[Cu][Cu].[O-]C(=O)C=CC=Cc1cc(C=CC=CC(=O)[O-])c(cc1C=CC=CC(=O)[O-])C=CC=CC(=O)[O-] MOFid-v1.ssa,nbo.cat0;ssa_sym_5_mc_2_sym_5_on_9_L_15	Cu.MTNSFCJUEJXWCD.MOFkey-v1.ssa
ssa_sym_5_mc_2_sym_5_on_9_L_21	[Cu][Cu].[O-]C(=O)c1ccc2c(c1)oc1c2ccc(c1)c1cc(c2ccc3c(c2)oc2c3ccc(c2)C(=O)[O-])c(cc1c1ccc2c(c1)oc1c2ccc(c1)C(=O)[O-])c1ccc2c(c1)oc1c2ccc(c1)C(=O)[O-] MOFid-v1.ssa,nbo.cat0;ssa_sym_5_mc_2_sym_5_on_9_L_21	Cu.PYSWIJNJENECII.MOFkey-v1.ssa
ssa_sym_5_mc_2_sym_5_on_9_L_4	[Cu][Cu].[O-]C(=O)[C]1NNC(=C1)c1cc(C2=C[C](NN2)C(=O)[O-])c(cc1C1=C[C](NN1)C(=O)[O-])C1=C[C](NN1)C(=O)[O-].[O-]C(=O)[C]1NNC(=C1)c1cc(C2=C[C](NN2)C(=O)[O-])c(cc1[C]1NNC(=C1)C(=O)[O-])C1=C[C](NN1)C(=O)[O-] MOFid-v1.ssa,nbo.cat0;ssa_sym_5_mc_2_sym_5_on_9_L_4	Cu.OHZYHVVXCLIDRX.MOFkey-v1.ssa
ssb_sym_5_mc_2_sym_5_on_9_L_15	[Cu][Cu].[O-]C(=O)C=CC=Cc1cc(C=CC=CC(=O)[O-])c(cc1C=CC=CC(=O)[O-])C=CC=CC(=O)[O-] MOFid-v1.ssb,pto.cat0;ssb_sym_5_mc_2_sym_5_on_9_L_15	Cu.MTNSFCJUEJXWCD.MOFkey-v1.ssb
ssb_sym_5_mc_2_sym_5_on_9_L_21	[Cu][Cu].[O-]C(=O)c1ccc2c(c1)oc1c2ccc(c1)c1cc(c2ccc3c(c2)oc2c3ccc(c2)C(=O)[O-])c(cc1c1ccc2c(c1)oc1c2ccc(c1)C(=O)[O-])c1ccc2c(c1)oc1c2ccc(c1)C(=O)[O-] MOFid-v1.ssb.cat0;ssb_sym_5_mc_2_sym_5_on_9_L_21	Cu.PYSWIJNJENECII.MOFkey-v1.ssb
ssb_sym_5_mc_2_sym_5_on_9_L_4	[Cu][Cu].[O-]C(=O)[C]1NNC(=C1)c1cc(C2=C[C](NN2)C(=O)[O-])c(cc1C1=C[C](NN1)C(=O)[O-])C1=C[C](NN1)C(=O)[O-] MOFid-v1.ssb.cat0;ssb_sym_5_mc_2_sym_5_on_9_L_4	Cu.OHZYHVVXCLIDRX.MOFkey-v1.ssb
tbo_sym_3_on_2_sym_5_mc_2_L_12	[Cu][Cu].[O-]C(=O)c1ccc(cc1)c1cc(cc(c1)c1ccc(cc1)C(=O)[O-])c1ccc(cc1)C(=O)[O-] MOFid-v1.tbo,pto.cat0;tbo_sym_3_on_2_sym_5_mc_2_L_12	Cu.SATWKVZGMWCXOJ.MOFkey-v1.tbo
tbo_sym_3_on_2_sym_5_mc_2_L_20	[Cu][Cu].[O-]C(=O)c1ccc(cc1)C#Cc1cc(C#Cc2ccc(cc2)C(=O)[O-])cc(c1)C#Cc1ccc(cc1)C(=O)[O-] MOFid-v1.rhr.cat0;tbo_sym_3_on_2_sym_5_mc_2_L_20	Cu.KKEYFWRCBNTPAC.MOFkey-v1.rhr
tbo_sym_3_on_2_sym_5_mc_2_L_24	[Cu][Cu].[O-]C(=O)c1ccc(cc1)c1ccc(cc1)c1cc(cc(c1)c1ccc(cc1)c1ccc(cc1)C(=O)[O-])c1ccc(cc1)c1ccc(cc1)C(=O)[O-] MOFid-v1.tbo,rhr.cat0;tbo_sym_3_on_2_sym_5_mc_2_L_24	Cu.PEQRGMPXYDIZSX.MOFkey-v1.tbo
tbo_sym_3_on_2_sym_5_mc_2_L_3	[Cu][Cu].[O-]C(=O)C#Cc1cc(C#CC(=O)[O-])cc(c1)C#CC(=O)[O-] MOFid-v1.tbo,rhr.cat0;tbo_sym_3_on_2_sym_5_mc_2_L_3	Cu.KHRUPMNUDNAAJH.MOFkey-v1.tbo

Henry Constants for Alkanes

Supplemental Table 2: Henry's constants for small alkanes in 38 selected MOFs at 300 K. Values are in units of mol/kg/Pa. MOFs are grouped by topology.

MOF	methane	ethane	propane	*n*-butane	isobutane
dia_L12	6.5E-06	1.6E-05	3.4E-05	7.6E-05	6.3E-05
dia_L20	7.2E-06	1.4E-05	2.7E-05	5.4E-05	4.5E-05
dia_L24	8.0E-06	1.7E-05	3.3E-05	7.0E-05	5.8E-05
dia_L3	5.4E-06	1.2E-05	2.4E-05	4.9E-05	4.2E-05
lcs_L12	6.3E-06	1.6E-05	3.7E-05	8.6E-05	7.1E-05
lcs_L20	6.9E-06	1.4E-05	2.7E-05	5.5E-05	4.6E-05
lcs_L24	7.7E-06	1.6E-05	3.3E-05	7.0E-05	5.8E-05
lcs_L3	5.3E-06	1.2E-05	2.5E-05	5.4E-05	4.6E-05
lvt_L12	7.2E-06	5.9E-05	4.4E-04	3.5E-03	3.4E-03
lvt_L20	4.9E-06	2.1E-05	7.1E-05	2.4E-04	2.1E-04
lvt_L24	5.1E-06	1.8E-05	5.2E-05	1.5E-04	1.4E-04
lvt_L3	3.9E-06	2.4E-05	1.3E-04	6.3E-04	6.3E-04
nbo_L12	1.6E-05	2.8E-04	2.0E-03	2.8E-02	1.9E-04
nbo_L20	4.1E-06	9.9E-06	2.1E-05	4.5E-05	3.9E-05
nbo_L24	5.1E-06	1.4E-05	3.6E-05	9.0E-05	8.1E-05
nbo_L3	2.4E-06	7.0E-06	1.7E-05	4.5E-05	4.0E-05
pto_L12	5.7E-06	2.1E-05	6.6E-05	2.1E-04	1.9E-04
pto_L20	5.4E-06	1.3E-05	2.7E-05	5.9E-05	5.1E-05
pto_L24	6.3E-06	1.6E-05	3.6E-05	8.5E-05	7.1E-05
pto_L3	4.0E-06	1.2E-05	3.3E-05	9.2E-05	8.1E-05
rhr_L20	4.6E-06	1.1E-05	2.6E-05	6.6E-05	5.9E-05
rhr_L12	4.8E-06	2.9E-05	2.3E-04	1.3E-03	2.3E-03
rhr_L24	5.9E-06	1.7E-05	4.7E-05	1.3E-04	1.1E-04
rhr_L3	2.8E-06	9.0E-06	2.1E-05	5.6E-05	2.4E-05
sod_L24	8.9E-06	1.8E-05	3.5E-05	7.1E-05	6.1E-05
sod_L12	6.9E-06	1.6E-05	3.4E-05	7.5E-05	6.2E-05
sod_L20	7.9E-06	1.5E-05	2.9E-05	5.7E-05	4.8E-05
sod_L3	5.9E-06	1.3E-05	2.6E-05	5.6E-05	4.8E-05
ssa_L15	6.2E-06	3.0E-05	1.3E-04	6.8E-04	4.7E-04
ssa_L21	6.6E-06	2.8E-05	1.1E-04	5.5E-04	4.5E-04
ssa_L4	6.2E-06	4.7E-05	2.8E-04	2.0E-03	1.5E-03
ssb_L15	5.6E-06	2.4E-05	8.4E-05	3.1E-04	1.8E-04
ssb_L21	6.2E-06	2.5E-05	9.7E-05	4.3E-04	3.7E-04
ssb_L4	4.9E-06	2.2E-05	8.2E-05	3.1E-04	2.7E-04
tbo_L12	5.6E-06	1.9E-05	5.7E-05	1.9E-04	1.5E-04
tbo_L20	6.0E-06	1.3E-05	2.8E-05	6.0E-05	5.2E-05
tbo_L24	7.2E-06	1.8E-05	4.1E-05	9.9E-05	8.9E-05
tbo_L3	4.0E-06	1.2E-05	3.6E-05	1.2E-04	1.1E-04

Supplemental Table 3: Henry's constants for small alkanes in 38 selected MOFs at 433 K. Values are in units of mol/kg/Pa. MOFs are group by topology.

MOF	methane	ethane	propane	*n*-butane	isobutane
dia_L12	2.7E-06	4.1E-06	6.1E-06	9.0E-06	8.4E-06
dia_L20	3.4E-06	4.7E-06	6.2E-06	8.5E-06	8.0E-06
dia_L24	3.8E-06	5.2E-06	7.1E-06	9.8E-06	9.2E-06
dia_L3	2.3E-06	3.5E-06	5.0E-06	7.1E-06	6.7E-06
lcs_L12	2.5E-06	4.0E-06	6.0E-06	9.2E-06	8.5E-06
lcs_L20	3.2E-06	4.5E-06	6.0E-06	8.3E-06	7.9E-06
lcs_L24	3.5E-06	5.0E-06	6.8E-06	9.6E-06	9.0E-06
lcs_L3	2.1E-06	3.4E-06	5.0E-06	7.3E-06	6.9E-06
lvt_L12	1.3E-06	4.9E-06	1.7E-05	6.2E-05	6.3E-05
lvt_L20	1.3E-06	3.0E-06	6.2E-06	1.3E-05	1.2E-05
lvt_L24	1.6E-06	3.4E-06	6.3E-06	1.2E-05	1.1E-05
lvt_L3	8.7E-07	2.6E-06	6.7E-06	1.7E-05	1.7E-05
nbo_L12	1.4E-06	5.6E-06	1.2E-05	3.6E-05	8.1E-06
nbo_L20	1.7E-06	2.6E-06	3.8E-06	5.5E-06	5.2E-06
nbo_L24	2.0E-06	3.3E-06	5.1E-06	7.8E-06	7.5E-06
nbo_L3	8.7E-07	1.6E-06	2.8E-06	4.8E-06	4.6E-06
pto_L12	1.8E-06	3.7E-06	7.1E-06	1.3E-05	1.3E-05
pto_L20	2.3E-06	3.5E-06	5.1E-06	7.4E-06	7.0E-06
pto_L24	2.7E-06	4.1E-06	6.2E-06	9.3E-06	8.7E-06
pto_L3	1.4E-06	2.7E-06	4.8E-06	8.8E-06	8.3E-06
rhr_L20	2.0E-06	3.0E-06	4.4E-06	6.5E-06	6.4E-06
rhr_L12	1.5E-06	3.3E-06	8.6E-06	2.1E-05	2.8E-05
rhr_L24	2.4E-06	3.8E-06	5.9E-06	9.4E-06	8.9E-06
rhr_L3	9.8E-07	1.7E-06	2.4E-06	3.7E-06	3.0E-06
sod_L24	4.4E-06	5.8E-06	7.7E-06	1.0E-05	9.90E-06
sod_L12	3.0E-06	4.4E-06	6.3E-06	9.2E-06	8.6E-06
sod_L20	3.9E-06	5.2E-06	6.8E-06	9.1E-06	8.6E-06
sod_L3	2.6E-06	3.8E-06	5.4E-06	7.8E-06	7.4E-06
ssa_L15	1.9E-06	3.9E-06	7.8E-06	1.7E-05	1.5E-05
ssa_L21	2.1E-06	4.0E-06	7.5E-06	1.5E-05	1.4E-05
ssa_L4	1.3E-06	3.5E-06	8.3E-06	2.2E-05	1.9E-05
ssb_L15	1.7E-06	3.5E-06	6.1E-06	1.1E-05	9.2E-06
ssb_L21	2.0E-06	4.0E-06	7.6E-06	1.5E-05	1.4E-05
ssb_L4	1.3E-06	3.0E-06	6.3E-06	1.3E-05	1.2E-05
tbo_L12	2.0E-06	3.7E-06	6.5E-06	1.2E-05	1.1E-05
tbo_L20	2.7E-06	3.9E-06	5.4E-06	7.8E-06	7.3E-06
tbo_L24	3.2E-06	4.7E-06	6.8E-06	1.0E-05	9.6E-06
tbo_L3	1.5E-06	2.7E-06	4.9E-06	9.1E-06	8.7E-06

Supplemental Table 4: Henry's constants for C5 and C6 alkanes in 38 selected MOFs at 300 K. Values are in units of mol/kg/Pa. MOFs are grouped by topology.

MOF	n-pentane	neopentane	2-methylbutane	*n*-hexane	2-methylpentane	3-methylpentane	2,2-dimethylbutane	2,3-dimethylbutane
dia_L_12	1.8E-04	5.9E-05	1.3E-04	4.0E-04	3.1E-04	2.8E-04	1.8E-04	2.3E-04
dia_L_20	1.1E-04	4.2E-05	8.6E-05	2.3E-04	1.8E-04	1.7E-04	1.1E-04	1.4E-04
dia_L_24	1.5E-04	5.3E-05	1.2E-04	3.3E-04	2.6E-04	2.3E-04	1.5E-04	2.0E-04
dia_L_3	1.0E-04	4.0E-05	8.1E-05	2.1E-04	1.7E-04	1.6E-04	1.1E-04	1.4E-04
lcs_L_12	2.1E-04	6.6E-05	1.6E-04	5.1E-04	3.9E-04	3.6E-04	2.2E-04	3.0E-04
lcs_L_20	1.2E-04	4.3E-05	9.0E-05	2.4E-04	1.9E-04	1.7E-04	1.2E-04	1.5E-04
lcs_L_24	1.6E-04	5.4E-05	1.2E-04	3.5E-04	2.7E-04	2.5E-04	1.5E-04	2.1E-04
lcs_L_3	1.2E-04	4.5E-05	9.3E-05	2.5E-04	2.1E-04	1.9E-04	1.3E-04	1.6E-04
lvt_L_12	2.5E-02	9.1E-03	3.0E-02	1.6E-01	1.9E-01	2.4E-01	2.0E-01	3.1E-01
lvt_L_20	8.7E-04	2.5E-04	6.8E-04	3.1E-03	2.5E-03	2.3E-03	1.5E-03	1.9E-03
lvt_L_24	4.3E-04	1.6E-04	3.8E-04	1.2E-03	1.1E-03	1.0E-03	7.4E-04	9.3E-04
lvt_L_3	3.1E-03	9.6E-04	2.9E-03	1.4E-02	1.4E-02	1.3E-02	9.5E-03	1.2E-02
nbo_L_12	4.2E-01	2.1E-04	7.9E-04	6.3E+00	4.5E-03	3.2E-03	1.4E-03	2.3E-03
nbo_L_20	9.7E-05	3.7E-05	8.1E-05	2.0E-04	1.8E-04	1.6E-04	1.2E-04	1.4E-04
nbo_L_24	2.2E-04	8.0E-05	1.9E-04	5.1E-04	4.4E-04	4.1E-04	3.0E-04	3.6E-04
nbo_L_3	1.2E-04	5.2E-05	1.0E-04	2.9E-04	2.8E-04	2.8E-04	2.1E-04	2.6E-04
pto_L_12	6.2E-04	2.4E-04	6.1E-04	1.7E-03	1.7E-03	1.8E-03	1.4E-03	1.8E-03
pto_L_20	1.3E-04	5.0E-05	1.1E-04	2.8E-04	2.4E-04	2.3E-04	1.6E-04	2.0E-04
pto_L_24	2.0E-04	6.8E-05	1.6E-04	4.7E-04	3.9E-04	3.7E-04	2.3E-04	3.2E-04
pto_L_3	2.5E-04	1.0E-04	2.2E-04	7.0E-04	6.2E-04	6.1E-04	4.4E-04	5.5E-04
rhr_L_20	1.8E-04	6.8E-05	1.6E-04	4.7E-04	5.2E-04	4.9E-04	3.3E-04	4.2E-04
rhr_L_12	4.8E-03	6.2E-03	1.2E-02	1.8E-02	3.2E-02	4.3E-02	9.2E-02	9.4E-02
rhr_L_24	3.8E-04	1.2E-04	3.1E-04	1.2E-03	9.4E-04	8.3E-04	5.5E-04	6.9E-04
rhr_L_3	1.5E-04	1.8E-05	5.4E-05	4.0E-04	1.6E-04	1.3E-04	5.3E-05	7.9E-05
sod_L_24	1.6E-04	5.7E-05	1.3E-04	3.4E-04	2.9E-04	2.7E-04	1.7E-04	2.2E-04
sod_L_12	1.8E-04	5.9E-05	1.3E-04	4.0E-04	3.2E-04	2.9E-04	1.8E-04	2.4E-04
sod_L_20	1.2E-04	4.5E-05	9.2E-05	2.5E-04	2.0E-04	1.8E-04	1.2E-04	1.5E-04
sod_L_3	1.3E-04	4.8E-05	1.0E-04	2.9E-04	2.3E-04	2.2E-04	1.4E-04	1.9E-04
ssa_L_15	3.7E-03	5.6E-04	2.4E-03	1.9E-02	1.4E-02	1.3E-02	6.3E-03	9.4E-03
ssa_L_21	2.9E-03	4.8E-04	2.4E-03	1.2E-02	1.3E-02	1.3E-02	6.6E-03	1.2E-02
ssa_L_4	1.6E-02	1.6E-03	1.1E-02	1.1E-01	1.0E-01	9.0E-02	3.4E-02	6.6E-02
ssb_L_15	1.2E-03	1.3E-04	5.9E-04	4.4E-03	2.5E-03	1.9E-03	8.0E-04	1.1E-03
ssb_L_21	1.8E-03	4.7E-04	1.8E-03	7.9E-03	7.2E-03	7.8E-03	5.0E-03	8.3E-03
ssb_L_4	1.2E-03	3.4E-04	1.0E-03	4.5E-03	4.0E-03	3.8E-03	2.5E-03	3.4E-03
tbo_L_12	6.5E-04	1.8E-04	5.1E-04	2.3E-03	1.9E-03	1.8E-03	1.0E-03	1.5E-03
tbo_L_20	1.3E-04	5.0E-05	1.1E-04	2.9E-04	2.5E-04	2.3E-04	1.6E-04	2.0E-04
tbo_L_24	2.4E-04	8.8E-05	2.1E-04	5.8E-04	5.0E-04	4.7E-04	3.4E-04	4.2E-04
tbo_L_3	4.2E-04	1.7E-04	3.9E-04	1.4E-03	1.5E-03	1.5E-03	1.1E-03	1.4E-03

Supplemental Table 5: Henry's constants for C5 and C6 alkanes in 38 selected MOFs at 433 K. Values are in units of mol/kg/Pa. MOFs are grouped by topology.

MOF	*n*-pentane	neopentane	2-methylbutane	*n*-hexane	2-methylpentane	3-methylpentane	2,2-dimethylbutane	2,3-dimethylbutane
dia_L_12	1.4E-05	8.2E-06	1.2E-05	2.0E-05	1.9E-05	1.8E-05	1.5E-05	1.7E-05
dia_L_20	1.2E-05	7.9E-06	1.1E-05	1.6E-05	1.5E-05	1.5E-05	1.3E-05	1.4E-05
dia_L_24	1.4E-05	9.0E-06	1.3E-05	2.0E-05	1.8E-05	1.8E-05	1.5E-05	1.7E-05
dia_L_3	1.0E-05	6.7E-06	9.6E-06	1.5E-05	1.4E-05	1.4E-05	1.2E-05	1.3E-05
lcs_L_12	1.4E-05	8.4E-06	1.3E-05	2.2E-05	2.0E-05	1.9E-05	1.6E-05	1.8E-05
lcs_L_20	1.2E-05	7.7E-06	1.1E-05	1.6E-05	1.5E-05	1.5E-05	1.3E-05	1.4E-05
lcs_L_24	1.4E-05	8.8E-06	1.3E-05	2.0E-05	1.8E-05	1.8E-05	1.5E-05	1.7E-05
lcs_L_3	1.1E-05	6.9E-06	1.0E-05	1.6E-05	1.5E-05	1.5E-05	1.2E-05	1.4E-05
lvt_L_12	2.0E-04	1.1E-04	2.4E-04	5.9E-04	7.1E-04	8.6E-04	8.1E-04	1.0E-03
lvt_L_20	2.6E-05	1.3E-05	2.4E-05	5.6E-05	5.1E-05	5.0E-05	4.0E-05	4.7E-05
lvt_L_24	2.1E-05	1.2E-05	2.0E-05	3.8E-05	3.5E-05	3.5E-05	3.0E-05	3.4E-05
lvt_L_3	3.9E-05	1.9E-05	3.9E-05	8.9E-05	8.9E-05	8.7E-05	7.6E-05	8.5E-05
nbo_L_12	1.2E-04	9.0E-06	1.8E-05	4.2E-04	4.2E-05	4.0E-05	2.9E-05	3.7E-05
nbo_L_20	8.0E-06	5.1E-06	7.5E-06	1.2E-05	1.1E-05	1.1E-05	9.3E-06	1.0E-05
nbo_L_24	1.2E-05	7.5E-06	1.1E-05	1.8E-05	1.7E-05	1.7E-05	1.5E-05	1.6E-05
nbo_L_3	8.3E-06	5.2E-06	8.0E-06	1.4E-05	1.4E-05	1.4E-05	1.2E-05	1.4E-05
pto_L_12	2.4E-05	1.4E-05	2.4E-05	4.3E-05	4.2E-05	4.4E-05	3.9E-05	4.5E-05
pto_L_20	1.1E-05	7.0E-06	1.0E-05	1.6E-05	1.5E-05	1.5E-05	1.3E-05	1.4E-05
pto_L_24	1.4E-05	8.7E-06	1.3E-05	2.2E-05	2.0E-05	2.0E-05	1.6E-05	1.9E-05
pto_L_3	1.6E-05	9.5E-06	1.5E-05	2.9E-05	2.8E-05	2.8E-05	2.3E-05	2.7E-05
rhr_L_20	1.0E-05	6.6E-06	1.0E-05	1.6E-05	1.7E-05	1.7E-05	1.4E-05	1.7E-05
rhr_L_12	4.2E-05	4.4E-05	6.7E-05	8.7E-05	1.1E-04	1.2E-04	2.0E-04	2.0E-04
rhr_L_24	1.5E-05	8.9E-06	1.4E-05	2.6E-05	2.4E-05	2.3E-05	1.9E-05	2.2E-05
rhr_L_3	5.8E-06	2.9E-06	4.5E-06	9.1E-06	7.2E-06	6.8E-06	5.4E-06	6.2E-06
sod_L_24	1.4E-05	9.7E-06	1.4E-05	1.9E-05	1.9E-05	1.9E-05	1.6E-05	1.8E-05
sod_L_12	1.4E-05	8.5E-06	1.3E-05	2.1E-05	1.9E-05	1.8E-05	1.5E-05	1.7E-05
sod_L_20	1.2E-05	8.5E-06	1.2E-05	1.7E-05	1.6E-05	1.6E-05	1.3E-05	1.5E-05
sod_L_3	1.1E-05	7.5E-06	1.1E-05	1.7E-05	1.6E-05	1.6E-05	1.3E-05	1.5E-05
ssa_L_15	4.1E-05	1.7E-05	3.5E-05	1.0E-04	8.9E-05	8.9E-05	6.4E-05	7.9E-05
ssa_L_21	3.1E-05	1.3E-05	2.9E-05	6.4E-05	6.1E-05	6.4E-05	4.4E-05	5.9E-05
ssa_L_4	6.0E-05	2.1E-05	5.4E-05	1.5E-04	1.5E-04	1.6E-04	1.0E-04	1.5E-04
ssb_L_15	2.1E-05	8.7E-06	1.6E-05	3.8E-05	3.1E-05	2.8E-05	2.1E-05	2.4E-05
ssb_L_21	3.1E-05	1.5E-05	2.9E-05	6.2E-05	5.9E-05	6.1E-05	5.0E-05	6.1E-05
ssb_L_4	2.8E-05	1.4E-05	2.6E-05	5.7E-05	5.3E-05	5.3E-05	4.2E-05	5.0E-05
tbo_L_12	2.3E-05	1.2E-05	2.1E-05	4.5E-05	4.2E-05	4.1E-05	3.2E-05	3.9E-05
tbo_L_20	1.1E-05	7.3E-06	1.1E-05	1.6E-05	1.5E-05	1.5E-05	1.3E-05	1.4E-05
tbo_L_24	1.5E-05	9.6E-06	1.4E-05	2.3E-05	2.1E-05	2.1E-05	1.8E-05	2.0E-05
tbo_L_3	1.8E-05	1.1E-05	1.8E-05	3.5E-05	3.6E-05	3.7E-05	3.1E-05	3.7E-05

Pore Size Distribution

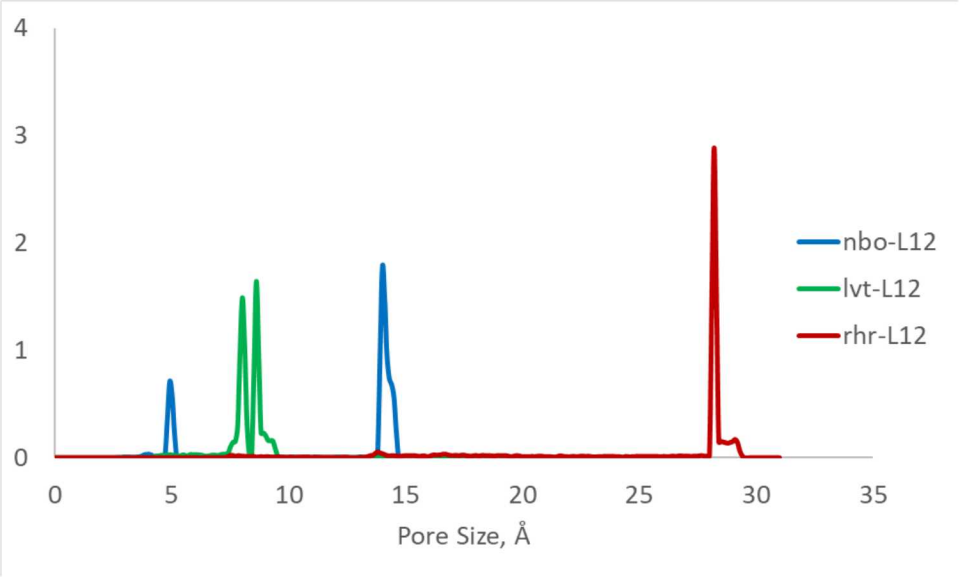

Supplemental Figure 2: Calculated pore size distribution for three selected polymorphs. Calculations were done using a probe with radius 1.8 Å which corresponds to a N_2 molecule.

Calculation of Free Energy

The Helmholtz free energy of adsorption at infinite dilution and the entropic contribution to the free energy were computed from Henry's constant calculations based on Widom insertions for alkanes in the three selected MOFs (nbo_L12, rhr_L12, and lvt_L12). The Helmholtz free energy was computed using:

$$\Delta A_{ads,i} = -RTln(RT\rho_s K_{H,i}) \qquad \text{Eq. S1}$$

where R is the gas constant (kJ/mol·K), T is the absolute temperature (K), ρ_s is the density of the sorbent in kg/m^3, and $K_{H,i}$ is the Henry's constant of a given isomer i in units of mol/kg/Pa. Note that 1 Pa = 1 J/m^3 = 0.001 kJ/m^3.

Equation S1 can be rewritten in terms of the enthalpy and entropy terms as follows:

$$\Delta A_{\mathrm{ads},i} = \Delta H_{\mathrm{ads},i} - T\Delta S_{\mathrm{ads},i} - RT \qquad \text{Eq. S2}$$

where $\Delta H_{\mathrm{ads},i}$ is the enthalpy of adsorption and $\Delta S_{\mathrm{ads},i}$ is the entropy of adsorption for isomer i. The enthalpic term can be decomposed into different contribution terms based on the type of interactions they represent as follows:

$$\Delta H_{\mathrm{ads},i} = \langle V_{\mathrm{gh},i}\rangle - \langle V_{\mathrm{h}}\rangle - \langle V_{\mathrm{g},i}\rangle + RT \qquad \text{Eq. S3}$$

where $\langle V_{\mathrm{gh},i}\rangle$ is the average potential energy from interactions between the guest molecules and host framework. This value is printed in the output file from RASPA in the Henry constant calculation. $\langle V_{\mathrm{h}}\rangle$ is the potential energy of the host framework, which is set to zero for rigid frameworks, as done in this

work. $\langle V_{g,i} \rangle$ is the average intramolecular potential energy of an isolated molecule of component i, which is obtained from a separate simulation of an isolated molecule in an empty box. Once $\Delta H_{ads,i}$ is known, the entropic term can be computed from the enthalpy and free energy from Equation S2:

$$-T\Delta S_{ads,i} = \Delta A_{ads,i} - \Delta H_{ads,i} + RT \qquad \text{Eq. S4}$$

The results from this analysis are shown in Supplemental Table 6 and Table 5

Supplemental Table 6: Thermodynamic data for adsorption of alkanes in selected MOFs at 433 K. Computed from Henry's coefficient calculations.

433 K	**ΔA_{ads} (kJ/mol)**			**ΔH_{ads} (kJ/mol)**			**$-T\Delta S_{ads}$ (kJ/mol)**		
	nbo_L12	**rhr_L12**	**lvt_L12**	**nbo_L12**	**rhr_L12**	**lvt_L12**	**nbo_L12**	**rhr_L12**	**lvt_L12**
methane	-5.3	-2.4	-4.9	-14.4	-5.7	-10.6	12.7	6.9	9.4
ethane	-10.2	-5.3	-9.6	-25.4	-12.2	-16.9	18.8	10.5	10.9
propane	-12.9	-8.7	-14.2	-33.0	-20.3	-22.9	23.6	15.2	12.4
***n*-butane**	-16.9	-12.0	-18.8	-44.8	-27.3	-29.0	31.6	19.0	13.9
isobutane	-11.5	-13.0	-18.8	-21.2	-30.1	-29.0	13.3	20.7	13.7
***n*-pentane**	-21.1	-14.4	-23.0	-56.1	-32.2	-35.0	38.6	21.3	15.6
neopentane	-11.9	-14.6	-20.9	-21.6	-34.6	-32.2	13.3	23.6	14.9
2-methylbutane	-14.4	-16.1	-23.7	-25.8	-36.8	-35.8	15.0	24.3	15.7
***n*-hexane**	-25.7	-17.0	-26.9	-69.4	-36.9	-40.9	47.2	23.5	17.6
2-methylpentane	-17.5	-17.8	-27.5	-30.3	-40.0	-41.3	16.5	25.8	17.3
3-methylpentane	-17.2	-18.3	-28.2	-29.5	-41.4	-41.7	15.8	26.7	17.1
2,2-dimethylbutane	-16.1	-20.1	-28.0	-27.4	-44.7	-41.2	14.8	28.2	16.8
2,3-dimethylbutane	-17.0	-20.1	-28.9	-28.8	-44.8	-42.4	15.4	28.3	17.1

Supplemental Table 7: Vapor pressures for alkanes at 300 K. Computed from Antoine equation parameters taken from NIST webbook.

Molecule	P_0 @ 300 K (bar)
n-pentane	0.73
n-hexane	0.22
neopentane	1.82
2-methylbutane	0.98
2-methylpentane	0.30
3-methylpentane	0.27
2,2-dimethylbutane	0.46
2,3-dimethylbutane	0.34

Supplemental Table 8: Loading at 1 bar and 433 K for C5 isomers in nbo_L12, lvt_L12, and rhr_L12. Values are in mol/kg.

MOF	nbo_L12	lvt_L12	rhr_L12
***n*-pentane**	1.30	1.13	0.56
2-methylbutane	0.56	1.29	0.71
neopentane	0.24	0.43	0.45

Snapshots of Adsorption in rhr_L12

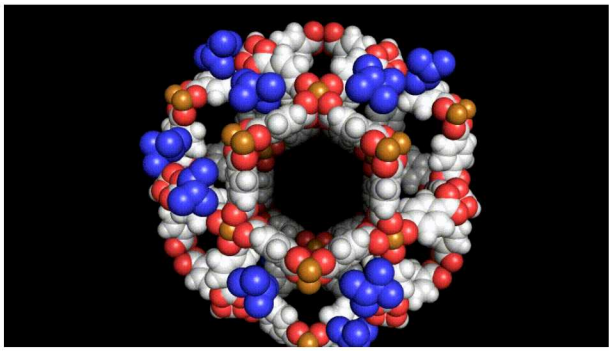

100 Pa
2,3-dimethylbutane

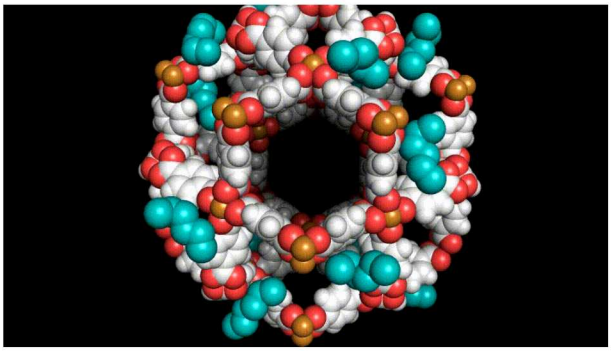

100 Pa
n-hexane

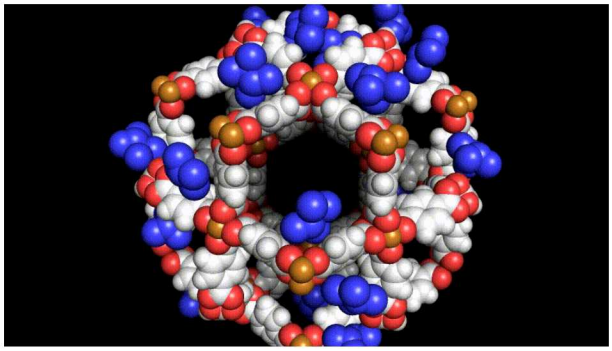

1000 Pa
2,3-dimethylbutane

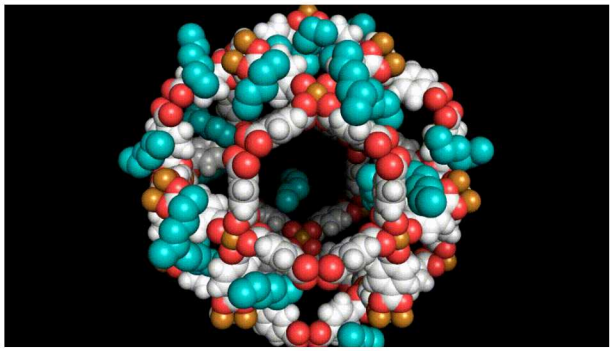

1000 Pa
n-hexane

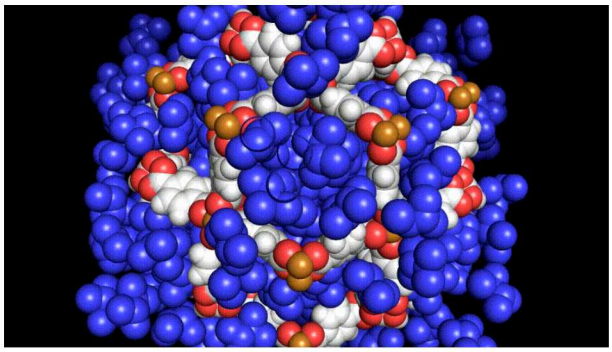

10000 Pa
2,3-dimethylbutane

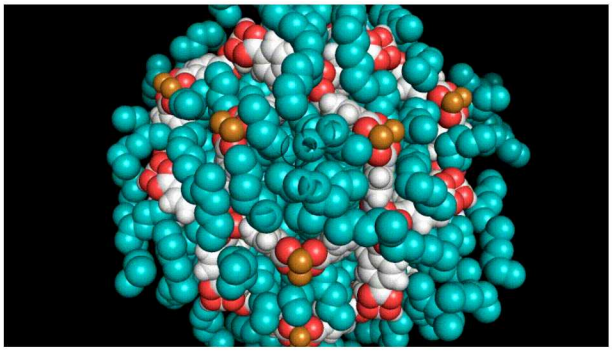

10000 Pa
n-hexane

Supplemental Figure 3: Snapshots from GCMC simulations of 2,3-dimethylbutane and n-hexane in rhr_L12 MOF at 300 K at 100, 1000, and 10000 Pa.

Effects of Composition on Selectivity

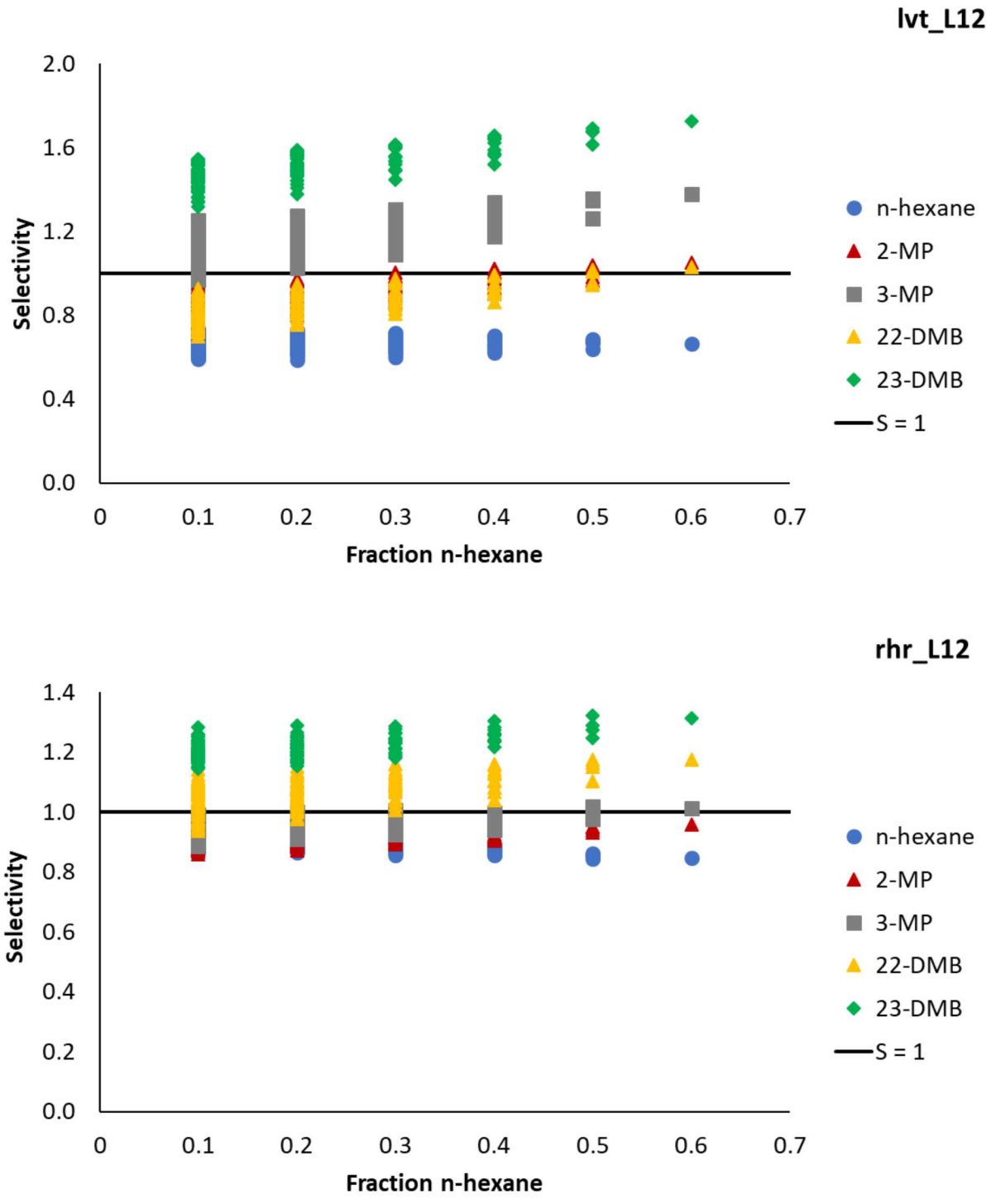

Supplemental Figure 4: Selectivity vs gas-phase composition for C6 alkanes in lvt_L12 and rhr_L12 at 433 K and 1 bar (total pressure). The horizontal axis represents the fraction of n-hexane in the gas phase. The vertical axis is the selectivity for the different components as computed using Eq. 1, and the black line indicates a selectivity (S) equal to 1.

nbo_L12 Conformations

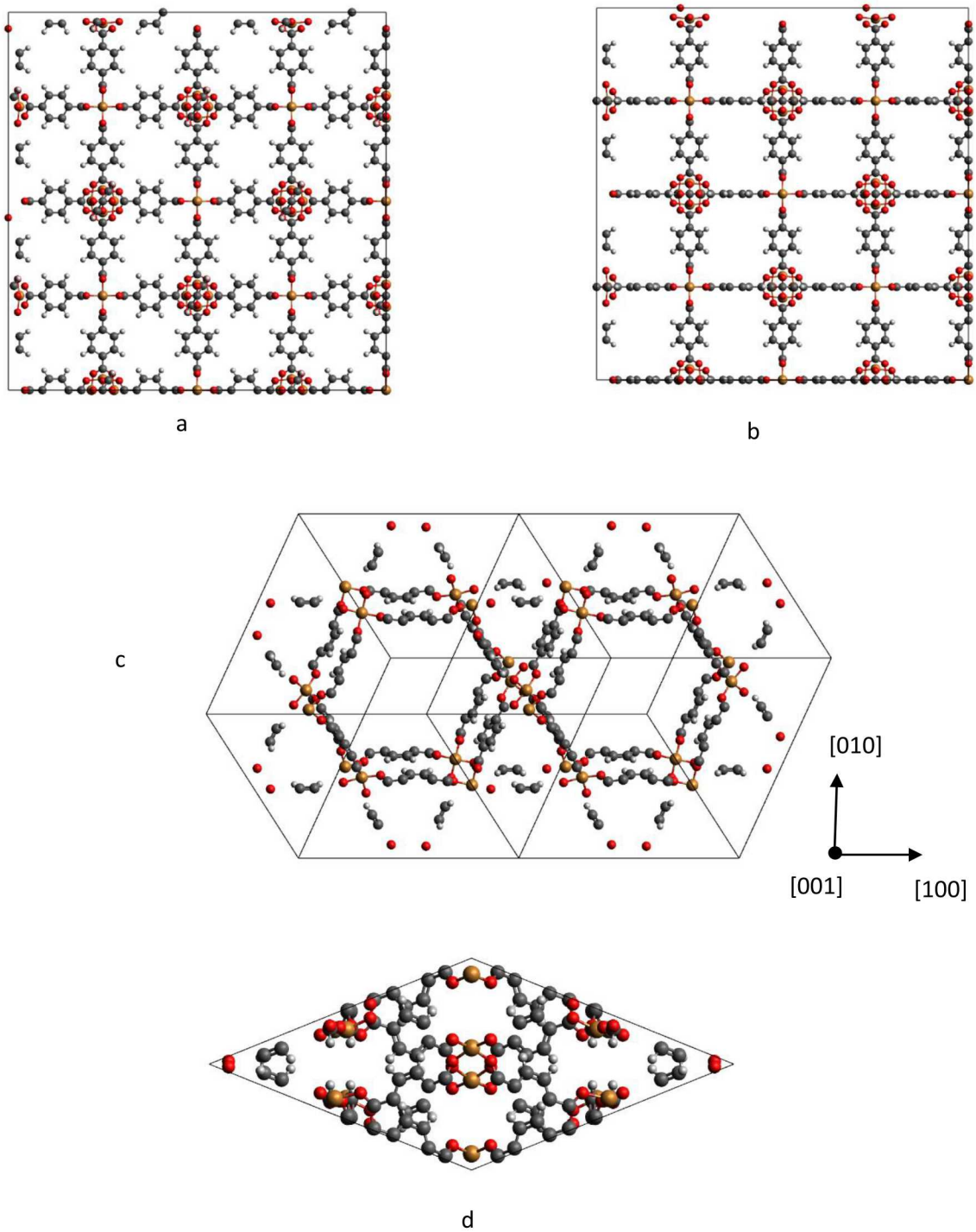

Supplemental Figure 5: Visualization of the nbo_L12 MOF in the a) cubic conformation along [001], b) cubic conformation along [110], c) star conformation along [001] and d) star conformation along [111]. Grey spheres are C, orange are Cu, red are O, and white are H